Article

Neuron

Role of Mitochondrial Metabolism in the Control of Early Lineage Progression and Aging Phenotypes in Adult Hippocampal Neurogenesis

Highlights

- Expression of mitochondrial complexes increases at the transition from NSC to IPC
- Genetic inhibition of mitochondrial function inhibits neurogenesis at IPC stage
- Mitochondrial dysfunction and aging produce similar neurogenesis phenotypes
- Enhancing mitochondrial function ameliorates age-related neurogenesis deficits

Authors

Ruth Beckervordersandforth, Birgit Ebert, Iris Schäffner, ..., Sebastian Jessberger, Hongjun Song, D. Chichung Lie

Correspondence

ruth.beckervordersandforth@fau.de (R.B.), chi.lie@fau.de (D.C.L.)

In Brief

Beckervordersandforth, Ebert et al. demonstrate that mitochondrial complex function functionally demarcates an early developmental step in adult hippocampal neurogenesis and identify mitochondrial dysfunction as a candidate target to counter age-associated neurogenesis deficits.

Beckervordersandforth et al., 2017, Neuron *93*, 560–573
February 8, 2017
http://dx.doi.org/10.1016/j.neuron.2016.12.017

CellPress

CellPress

Neuron
Article

Role of Mitochondrial Metabolism in the Control of Early Lineage Progression and Aging Phenotypes in Adult Hippocampal Neurogenesis

Ruth Beckervordersandforth,[1,10,*] Birgit Ebert,[1,2,10] Iris Schäffner,[1] Jonathan Moss,[3] Christian Fiebig,[1] Jaehoon Shin,[4] Darcie L. Moore,[5] Laboni Ghosh,[5] Mariela F. Trinchero,[6] Carola Stockburger,[7] Kristina Friedland,[7] Kathrin Steib,[2] Julia von Wittgenstein,[1] Silke Keiner,[8] Christoph Redecker,[8] Sabine M. Hölter,[2] Wei Xiang,[1] Wolfgang Wurst,[2] Ravi Jagasia,[2,9] Alejandro F. Schinder,[6] Guo-li Ming,[4] Nicolas Toni,[3] Sebastian Jessberger,[5] Hongjun Song,[4] and D. Chichung Lie[1,11,*]

[1]Institute of Biochemistry, Emil Fischer Center, Friedrich-Alexander Universität Erlangen-Nürnberg, 91054 Erlangen, Germany
[2]Institute of Developmental Genetics, Helmholtz Center Munich, German Research Center for Environmental Health, 85764 Munich-Neuherberg, Germany
[3]Department of Fundamental Neuroscience, University of Lausanne, 1005 Lausanne, Switzerland
[4]Institute for Cell Engineering, Department of Neurology, The Solomon Snyder Department of Neuroscience, Johns Hopkins University School of Medicine, Baltimore, MD 21205, USA
[5]Brain Research Institute, Faculty of Medicine and Science, University of Zurich, 8057 Zurich, Switzerland
[6]Laboratory of Neuronal Plasticity, Leloir Institute (IIBBA, CONICET), C1405BWE Buenos Aires, Argentina
[7]Molecular and Clinical Pharmacy, Friedrich-Alexander Universität Erlangen-Nürnberg, 91054 Erlangen, Germany
[8]Hans Berger Department of Neurology, Jena University Hospital, 07747 Jena, Germany
[9]F. Hoffmann-La Roche Ltd, CNS Discovery; Pharma Research and Early Development, 4070 Basel, Switzerland
[10]Co-first author
[11]Lead contact
*Correspondence: ruth.beckervordersandforth@fau.de (R.B.), chi.lie@fau.de (D.C.L.)
http://dx.doi.org/10.1016/j.neuron.2016.12.017

SUMMARY

Precise regulation of cellular metabolism is hypothesized to constitute a vital component of the developmental sequence underlying the life-long generation of hippocampal neurons from quiescent neural stem cells (NSCs). The identity of stage-specific metabolic programs and their impact on adult neurogenesis are largely unknown. We show that the adult hippocampal neurogenic lineage is critically dependent on the mitochondrial electron transport chain and oxidative phosphorylation machinery at the stage of the fast proliferating intermediate progenitor cell. Perturbation of mitochondrial complex function by ablation of the mitochondrial transcription factor A *(Tfam)* reproduces multiple hallmarks of aging in hippocampal neurogenesis, whereas pharmacological enhancement of mitochondrial function ameliorates age-associated neurogenesis defects. Together with the finding of age-associated alterations in mitochondrial function and morphology in NSCs, these data link mitochondrial complex function to efficient lineage progression of adult NSCs and identify mitochondrial function as a potential target to ameliorate neurogenesis-defects in the aging hippocampus.

INTRODUCTION

Quiescent radial glia-like neural stem cells (NSCs) in the rodent hippocampal dentate gyrus (DG) give rise to neurons throughout life. It is now well accepted that a substantial number of new neurons is also generated in the DG of adult humans (Eriksson et al., 1998; Spalding et al., 2013). New neurons fulfill important functions in hippocampal plasticity and it is hypothesized that impaired neurogenesis contributes to the pathophysiology of cognitive symptoms in aging and neuropsychiatric diseases (Abrous and Wojtowicz, 2015; Christian et al., 2014; Rolando and Taylor, 2014).

Neurogenesis from a quiescent radial glia-like NSC is achieved through a stereotypic developmental sequence controlled by the interplay of neurogenic niche-derived signals with intracellular pathways (Bond et al., 2015). To date, studies have largely focused on developmental signaling, transcriptional, and epigenetic pathways to understand how the neurogenic sequence is regulated (Aimone et al., 2014).

En route to its differentiation into a mature neuron, the quiescent NSC undergoes extensive changes in proliferative activity, cellular growth, and synaptic activity (Shin et al., 2015). These changes are likely to impose distinct demands on the availability of energy equivalents and precursors for anabolic pathways. The discovery that a metabolic shift toward de novo lipogenesis is required for the activation of quiescent NSCs and NSC proliferation provided the first direct evidence that lineage progression in adult hippocampal neurogenesis is functionally coupled to the activity of a specific metabolic program (Knobloch et al., 2013). The questions whether the adult neurogenic sequence

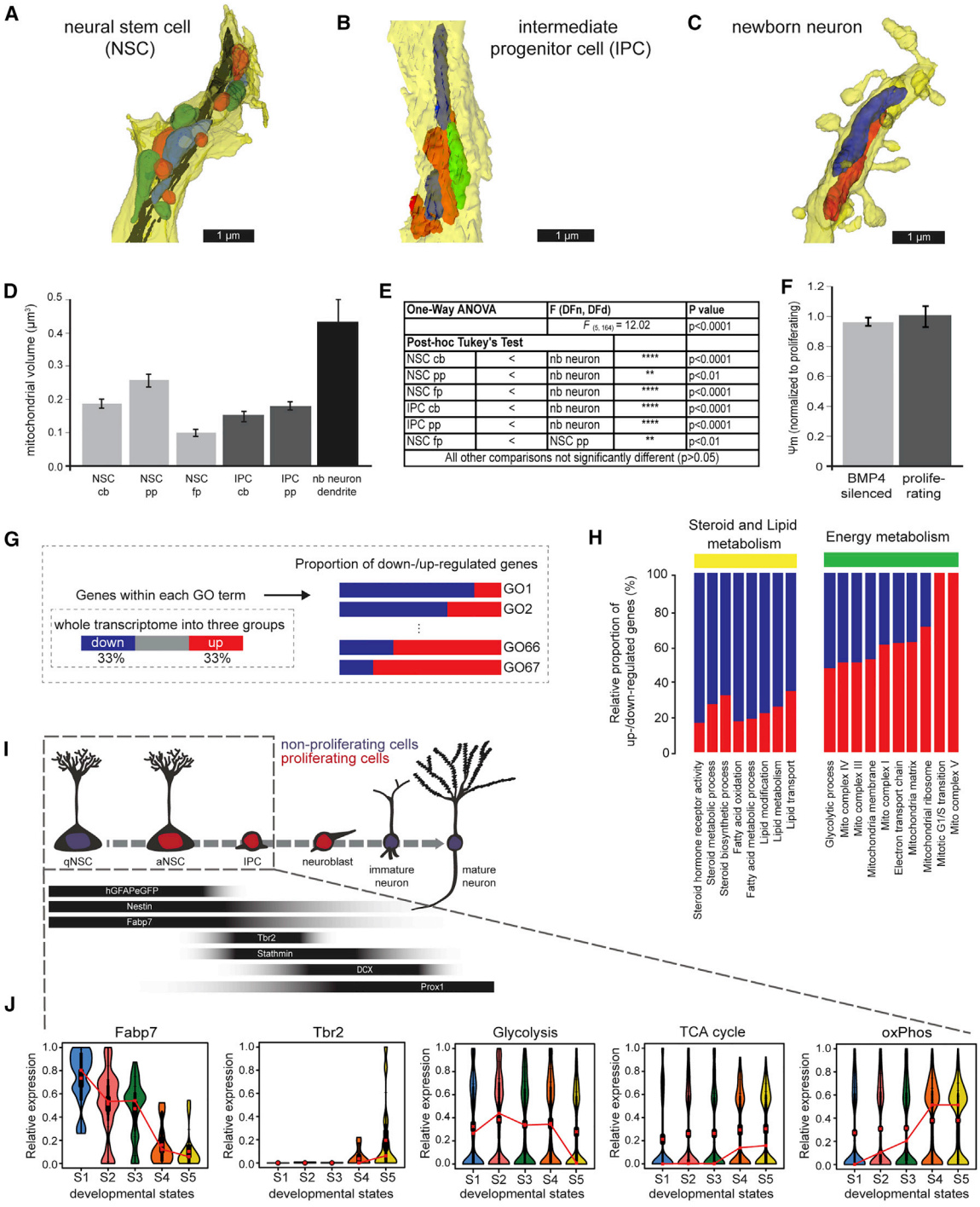

One-Way ANOVA	F (DFn, DFd)	P value
	$F_{(5, 164)} = 12.02$	p<0.0001
Post-hoc Tukey's Test		
NSC cb < nb neuron	****	p<0.0001
NSC pp < nb neuron	**	p<0.01
NSC fp < nb neuron	****	p<0.0001
IPC cb < nb neuron	****	p<0.0001
IPC pp < nb neuron	****	p<0.0001
NSC fp < NSC pp	**	p<0.01
All other comparisons not significantly different (p>0.05)		

Figure 1. Morphological EM Analysis of Mitochondria and Stage-Specific Molecular Program Suggests Adaptation of Metabolic Circuits

(A–C) Reconstruction of serial electron microscope (EM) sections of immunoperoxidase- or immunogold-labeled cells: (A) radial glial NSC primary process; (B) process of an intermediate progenitor cell (IPC); (C) segment of a month-old newborn (nb) neuron dendrite. Individual mitochondria were labeled in different colors to better illustrate their shape.

(D) Quantification of the average mitochondrial volume revealed that mitochondria in newborn neurons are larger than in NSCs and IPCs. Though mitochondria of newborn neurons appear small in cross-sections, their volumes are much larger due to their wider and highly elongated morphology (see also Movies S1, S2, and S3). The average mitochondrial volume in NSCs and IPCs is comparable with the exception of mitochondria in the primary process of NSCs (primary process, pp; fine process, fp; cell body, cb).

(E) Statistics of the comparative analysis of mitochondrial volume measurements.

(legend continued on next page)

is defined by developmental stage-specific metabolic codes, and whether metabolic programs constrain further steps in adult neurogenesis, remain unresolved.

Quiescent radial glia-like NSCs share many characteristics of astrocytes (Rolando and Taylor, 2014), which have a predominantly glycolytic profile (Bélanger et al., 2011; Hamberger and Hyden, 1963; Hyden and Lange, 1962). Notably, recent studies indicated that highly proliferative embryonic neural precursors are glycolytic (Agathocleous et al., 2012; Homem et al., 2014; Khacho et al., 2016; Zheng et al., 2016). In contrast, functionally integrated neurons are highly dependent on the mitochondrial electron transport chain (ETC) and oxidative phosphorylation (oxPhos) (Hall et al., 2012) to meet their high-energy requirements imposed in particular by presynaptic vesicle recycling, and by the recurrent generation of action potentials and postsynaptic potentials (Alle et al., 2009; Attwell and Laughlin, 2001). If and when a metabolic program involving ETC and oxPhos function becomes critical during in vivo mammalian neurogenesis in general, and in adult hippocampal neurogenesis in particular, remains unknown. Here, we made the surprising observation that integrity of the ETC and oxPhos machinery is critical already during the earliest stages of adult hippocampal neurogenesis long before the stage of synaptic integration of newborn neurons. Using pharmacologic and genetic approaches, we show that ETC and oxPhos function are critical for proliferation and survival of intermediate progenitor cells (IPCs) generated by activated NSCs. Moreover, we found evidence that impaired mitochondrial function contributes to age-associated decline in hippocampal neurogenesis and observed that pharmacological enhancement of mitochondrial function promotes neurogenesis in the aging hippocampus. Collectively, the present data identify activity of the ETC and oxPhos machinery as a critical determinant of adult hippocampal neurogenesis and indicate mitochondrial function as a candidate target to ameliorate age-associated neurogenesis deficits.

RESULTS

Increased mitochondrial mass and size are considered structural correlates of higher ETC and oxPhos activity (Alirol and Martinou, 2006). Ultra-structural analysis using electron microscopy revealed that mitochondria in adult hippocampal radial glia-like NSCs were of mixed globular and tubular shape (Figure 1A and Movie S1). In comparison, mitochondria in IPCs displayed a thin and more elongated shape (Figure 1B and Movie S2), while mitochondria in mature adult-born dentate granule neurons featured a wider and highly elongated morphology (Figure 1C and Movie S3). Mitochondria in different compartments of NSCs and IPCs were of comparable volume with the exception of mitochondria in the radial process of NSCs, which were slightly larger (Figures 1D and 1E). Consistent with the long-standing notion that mature neurons are heavily reliant on ETC and oxPhos activity (Bélanger et al., 2011), and with the recent in vitro and ex vivo evidence that proliferating neural progenitor cells show high levels of aerobic glycolysis (Agathocleous et al., 2012; Homem et al., 2014; Khacho et al., 2016; Zheng et al., 2016), mitochondria in neurons were significantly more voluminous than mitochondria in NSCs and IPCs (Figures 1D and 1E).

Using cultured adult neural stem/progenitor cells (NSPCs), we found that mitochondrial membrane potential, measured using rhodamine 123, did not significantly differ between BMP4-induced quiescent NSPCs (Martynoga et al., 2013; Mira et al., 2010) and proliferating NSPCs (Figure 1F). In line with recent in vitro analyses of embryonic NSPCs (Khacho et al., 2016; Zheng et al., 2016), neuronally differentiated NSPCs displayed a significantly increased mitochondrial membrane potential compared to proliferating NSPCs (data not shown) indicating higher ETC and oxPhos activity in NSPC-derived neurons.

To gain further insight into the timing of increased ETC and oxPhos activity during the generation of neurons from radial glia-like NSCs in vivo, we analyzed gene expression datasets from the adult hippocampal neurogenic lineage with a focus on genes linked to metabolism. Counter to the mitochondrial morphology and membrane potential measurements, in-depth analysis of a resource describing the transcriptomic dynamics during the early phases of adult hippocampal neurogenesis (Shin et al., 2015) indicated an unexpected increase of ETC and oxPhos activity already in the early neurogenic lineage (Figures 1G–1J, and Figure S1). Upregulation of cell-cycle genes reflected the activation of quiescent NSCs and the increasing proliferative activity along the early neurogenic lineage (Figure S1A). Transcriptomic signatures suggested beta-oxidation and glycolysis as energy-providing metabolic circuits in quiescent and activated NSCs (Figures 1H and 1J). Downregulation of the NSC marker *Fabp7* (Lugert et al., 2010; Steiner et al., 2006) and expression of the IPC marker *Tbr2* (Hodge et al., 2012) were paralleled by upregulation of enzymes of the tricarboxylic acid (TCA) cycle (Figure 1J), which provides electron carriers to the ETC, and upregulation of components of the mitochondrial (mt) complexes,

(F) In vitro quiescent NSPCs (BMP4-silenced as described in STAR Methods) exhibit a membrane potential comparable to the membrane potential of proliferating NSPCs.

(G) Scheme of the GO enrichment analysis of the transcriptomic database described in (Shin et al., 2015). The total genes in the genome were first divided into three groups based on their trend along pseudotime progression. The proportion of up and down genes in each GO entity of interest was surveyed to evaluate the functional directionality of the GO entity during progression of early adult neurogenesis.

(H) Proportion of upregulated and downregulated genes within key functional GO entities (see also Figure S1A). Note the upregulation of ETC and mitochondrial complex associated genes.

(I) Schematic drawing of the hippocampal NSC lineage with stage-specific expression of molecular markers. Box indicates developmental stages covered by transcriptomic resource.

(J) Violin diagrams depict lineage progression of quiescent NSCs (qNSCs; aNSC, activated neural stem cell) to IPCs as evidenced by downregulation of *Fapb7* and concomitant upregulation of *Tbr2*. Note the downregulation of genes associated with glycolysis and upregulation of genes associated with the TCA cycle and oxPhos. S1–S5 represent developmental stages ordered along pseudotime progression. Data in (D) and (F) represented as mean ± SEM; t test was performed to test significance in membrane potential (F).

which are the structural prerequisites for ETC and oxPhos (Figures 1H and 1J). Most notably, genes related to mt complex V, i.e., the key enzymatic complex for mitochondrial ATP production/oxPhos, showed consistent upregulation during early lineage progression (Figures S1B–S1G). In contrast, key enzymes in glycolysis such as *aldolase A* and *lactate dehydrogenase A*, and the *mitochondrial uncoupling protein 2 (UCP2)*, which was recently implied in promoting aerobic glycolysis over oxPhos in embryonic neural precursor cells (Khacho et al., 2016; Zheng et al., 2016), were downregulated around the time of NSC activation (Figures S1H–S1K). Collectively, these results predicted a metabolic shift involving increased activity of ETC and oxPhos around the time of transition from activated NSCs to IPCs.

To test the functional relevance of the ETC and oxPhos machinery in the early neurogenic lineage, we interrupted ETC and oxPhos activity in NSPC cultures using rotenone, which inhibits the transfer of electrons from mt complex I to the electron carrier ubiquinone, and oligomycin, which inhibits mt complex V and thus oxPhos. NSPCs were treated with either compound for 24 hr prior to analysis. Both rotenone and oligomycin treatment reduced mitochondrial membrane potential to approximately 50% of control levels, demonstrating that NSPCs harbored a functional ETC (Figure 2A). Moreover, rotenone treatment significantly reduced ATP production, whereas oligomycin treatment almost completely blocked ATP production (Figure 2B). Most importantly, both treatments abolished cell proliferation (Figure 2C) and led to an approximately 5-fold increase in cell death (Figure 2D). These results revealed that proliferating NSPCs are highly dependent on functional ETC and oxPhos.

Next, we genetically disrupted mitochondrial ETC and oxPhos activity in NSPCs by conditional ablation of the *mitochondrial transcription factor A (Tfam)* (Larsson et al., 1998). Tfam is required for expression of key components of the mt complexes. As a consequence, ablation of *Tfam* produces profound dysfunction of the ETC and the oxPhos machinery (Larsson et al., 1998). NSPCs were isolated from the hippocampus of young adult mice harboring conditional *Tfam* alleles ($Tfam^{loxP/loxP}$) and were transduced with either a recombinant GFP-encoding mouse moloney leukemia virus (MMLV) or a recombinant MMLV bi-cistronically encoding for GFP and Cre-recombinase. Given the lack of suitable antibodies for immunohistochemical detection of Tfam, we performed genotyping PCRs to validate recombination of the conditional *Tfam* locus in GFP/Cre-virus transduced $Tfam^{loxP/loxP}$ NSPCs. PCR analysis revealed successful recombination of the conditional *Tfam* locus in a subset of NSPCs (Figure 2E). Moreover, *Tfam* conditional knockout ($Tfam^{cko}$) cultures showed a significant decrease in membrane potential and ATP production (Figures 2F and 2G), demonstrating the functional impact of *Tfam* deletion on ETC and oxPhos function. Despite multiple rounds of viral transduction, we were unable to obtain cultures that were highly enriched for *Tfam*-deleted NSPCs, which suggested possible defects in cell proliferation or viability of *Tfam*-depleted NSPCs. To measure proliferation and cell viability, we performed Bromodeoxyuridine (BrdU)-incorporation assays and Trypan-blue assays, respectively, of $Tfam^{cko}$ and control cultures. Using GFP-expression to identify GFP/Cre-virus ($Tfam^{cko}$ cultures) and GFP-virus (control cultures)-transduced cells, we found a significant reduction in proliferation (Figure 2H) and a substantial impairment in cell viability (Figure 2I) of *Tfam*-depleted NSPCs.

To explore whether and at what stage activity of mt complexes becomes essential in the adult hippocampal neurogenic lineage, we crossed $Tfam^{loxP/loxP}$ mice with $GLAST::CreER^{T2}$ mice (Mori et al., 2006) and *CAG-CAT-EGFP* reporter mice (Nakamura et al., 2006) to generate $Tfam^{cko}$ mice, which allow for Tamoxifen-dependent induction of mt complex dysfunction in radial glia-like NSCs. $GLAST::CreER^{T2}$*; CAG-CAT-EGFP* mice served as controls. A number of studies have found that *Tfam* conditional knockout mice almost invariably develop a phenotype only after weeks to months following disruption of the *Tfam* locus, most likely owing to the long half-life of *Tfam* transcripts, Tfam protein, and Tfam targets (Ekstrand et al., 2007; Silva et al., 2000; Sörensen et al., 2001; Wang et al., 1999). To study the impact of *Tfam*-deletion on neurogenesis in young adult mice, we therefore gave Tamoxifen injections to $Tfam^{cko}$ and control mice animals already on postnatal days 14, 16, and 18. We first sought to validate the deletion of *Tfam*. Because of the lack of suitable antibodies for immunohistochemical detection of Tfam, GFP-reporter expression and genotyping PCRs were used as proxies to determine recombination in Tamoxifen-treated $Tfam^{cko}$ mice (Figure S2A). Immunohistochemical analysis of mitochondria using antibodies against the mitochondrial chaperone HSP60, whose expression is Tfam independent, and against the mt respiratory complex IV component Cox1 (i.e., cytochrome *c* oxidase subunit 1), whose expression requires Tfam, provided additional evidence for *Tfam* deletion (Figures 2J–2M). Starting at the age of 4 months, a large fraction of recombined cells in $Tfam^{cko}$ mice contained $HSP60^{+}$ $Cox1^{-}$ mitochondria (65%; Figures 2K and 2M; Figure S2B). In contrast, $HSP60^{+}$ mitochondria in recombined cells of control mice were invariably positive for Cox1 (Figures 2J and 2L). In addition, many recombined cells in $Tfam^{cko}$ mice harbored mitochondria that showed increased HSP60-immunoreactivity and displayed an aberrant clumpy morphology (Figures 2K and 2M). Such aberrant mitochondrial phenotype was particularly prominent in NSCs ($Tfam^{cko}$ versus control: 100% versus <5%) but was also observable in newborn neurons ($Tfam^{cko}$ versus control: 58% versus 0%). Collectively, these data indicate that the conditional *Tfam* locus was successfully recombined and suggest—consistent with other studies—delayed mitochondrial impairment following in vivo ablation of *Tfam*.

$Tfam^{cko}$ mice were viable, showed no macroscopic differences in brain size and hippocampal morphology (Figures S2C and S3) and appeared healthy beyond the age of 24 months (data not shown). Consistent with the timing of immunohistochemical evidence for mitochondrial dysfunction, we observed a severe reduction in the density of recombined cells in the DG of $Tfam^{cko}$ mice starting at the age of 4 months, suggesting that *Tfam* deficiency impaired the generation and survival of new hippocampal neurons at this time point. Short-term BrdU pulse-chase experiments (single pulse of BrdU, 3 hr chase) showed that cell proliferation in the DG was unaffected in 2-month-old $Tfam^{cko}$ mice (Figure S2D). Long-term BrdU pulse-chase experiments (3 days pulse of BrdU at the age of 2 months, 2 months chase), however, revealed that cells generated at the age of 2 months

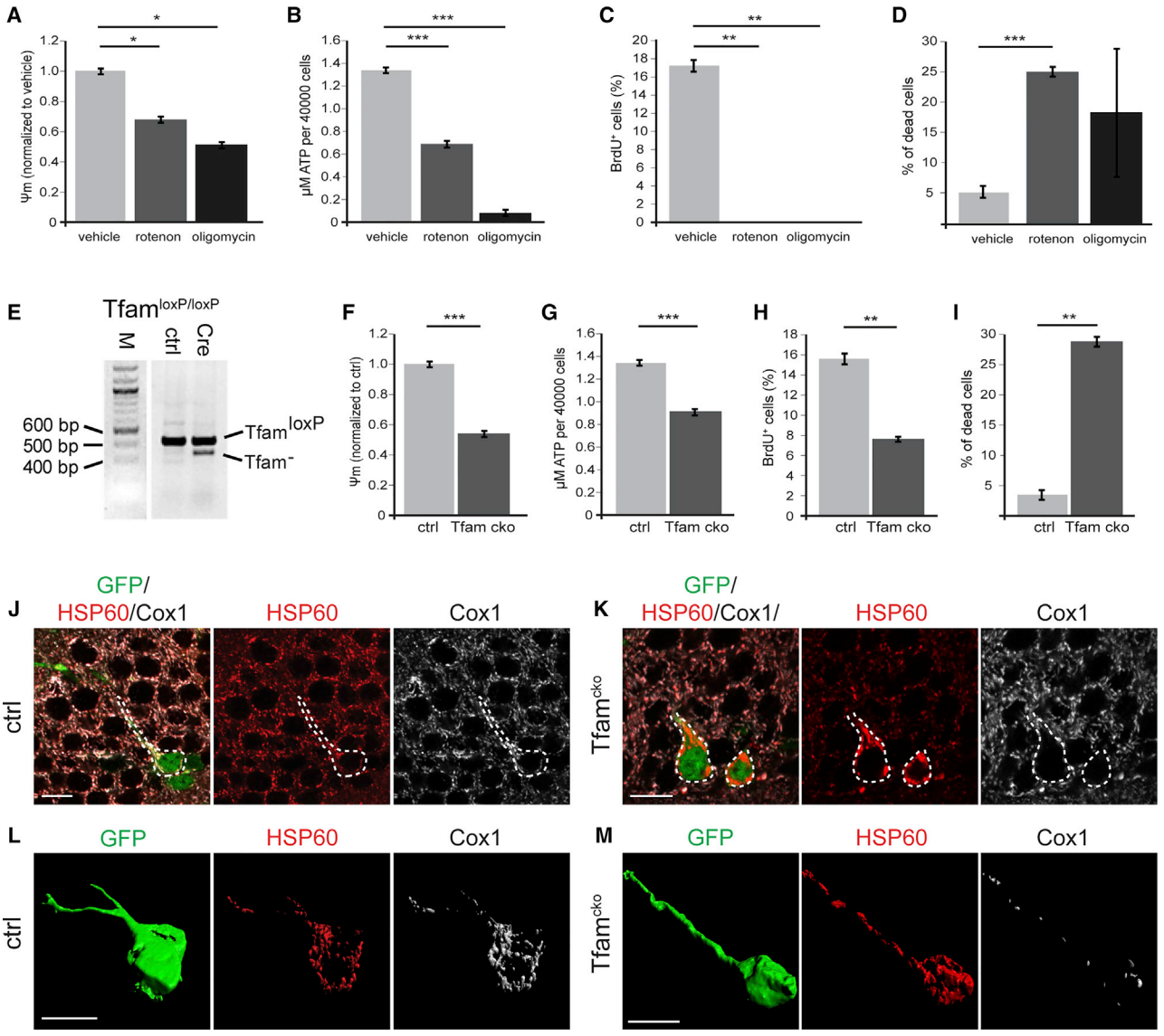

Figure 2. Pharmacological and Genetic Inhibition of ETC and oxPhos and Its Impact on NSPC Function In Vitro and Mitochondria In Vivo

(A–D) Blocking mitochondrial complex I and V by rotenone and oligomycin, respectively, leads to a significant decrease in membrane potential (A) and ATP content (B); rotenone and oligomycin treatment almost completely abolish cell proliferation (C) and increase cell death (D).

(E) Genotyping PCR of the *Tfam* locus of *Tfam*$^{fl/fl}$ NSPCs transduced with either a GFP-encoding control MMLV (ctrl) or an MMLV encoding for GFP and Cre-recombinase (Cre) reveals recombination of the conditional *Tfam* locus in the context of the GFP/Cre encoding MMLV. Note the presence of the *Tfam*^{loxP} PCR product in GFP/Cre transduced NSPCs, which indicates that recombination of the conditional *Tfam* locus was present only in a subpopulation of NSPCs.

(F–I) *Tfam*^{cko} NSPC cultures displayed a significant decrease in membrane potential (F) and ATP production (G) compared to control cells (ctrl); proliferation was significantly decreased (H) and cell death increased (I).

(J–M) Immunostaining for the mitochondrial proteins HSP60 (red) and Cox1 (white); GFP (green) served to identify recombined cells (outlined by white dotted line). (L and M) Reconstruction of recombinant ctrl and *Tfam*^{cko} cells. All cells contained HSP60^{+} mitochondria, but only in ctrl cells, mitochondria invariably co-expressed Cox1 (J and L); in *Tfam*^{cko} mice, recombinant cells showed strongly diminished Cox1 expression and displayed aberrant mitochondrial morphology (K and M). Data represented as mean ± SEM; t test was performed to determine significance; all scale bars = 10 µm.

were severely impaired in their long-term survival (Figure S2E). Moreover, 4-month-old *Tfam*^{cko} mice exhibited a pronounced proliferation deficit in the DG (Figures 3A, 3B, and 3F; Figure S2F). Using distinct histological markers for different precursor populations (Figure 1I), we performed quantitative analysis to determine whether *Tfam* deficiency impaired neurogenesis at a specific developmental stage. The total number of radial glial-like NSCs (Nestin^{+}) and activated NSCs (Nestin^{+}/MCM2^{+}) was comparable between the experimental groups (NSCs: p = 0.45; activated NSCs: p = 0.35; Figures 3C, 3G, and 3H), while the number of Tbr2^{+} IPCs (Figures 3D and 3I) and of doublecortin (DCX)$^{+}$ neuroblast and immature neuron progeny (Figures 3E and 3J) was

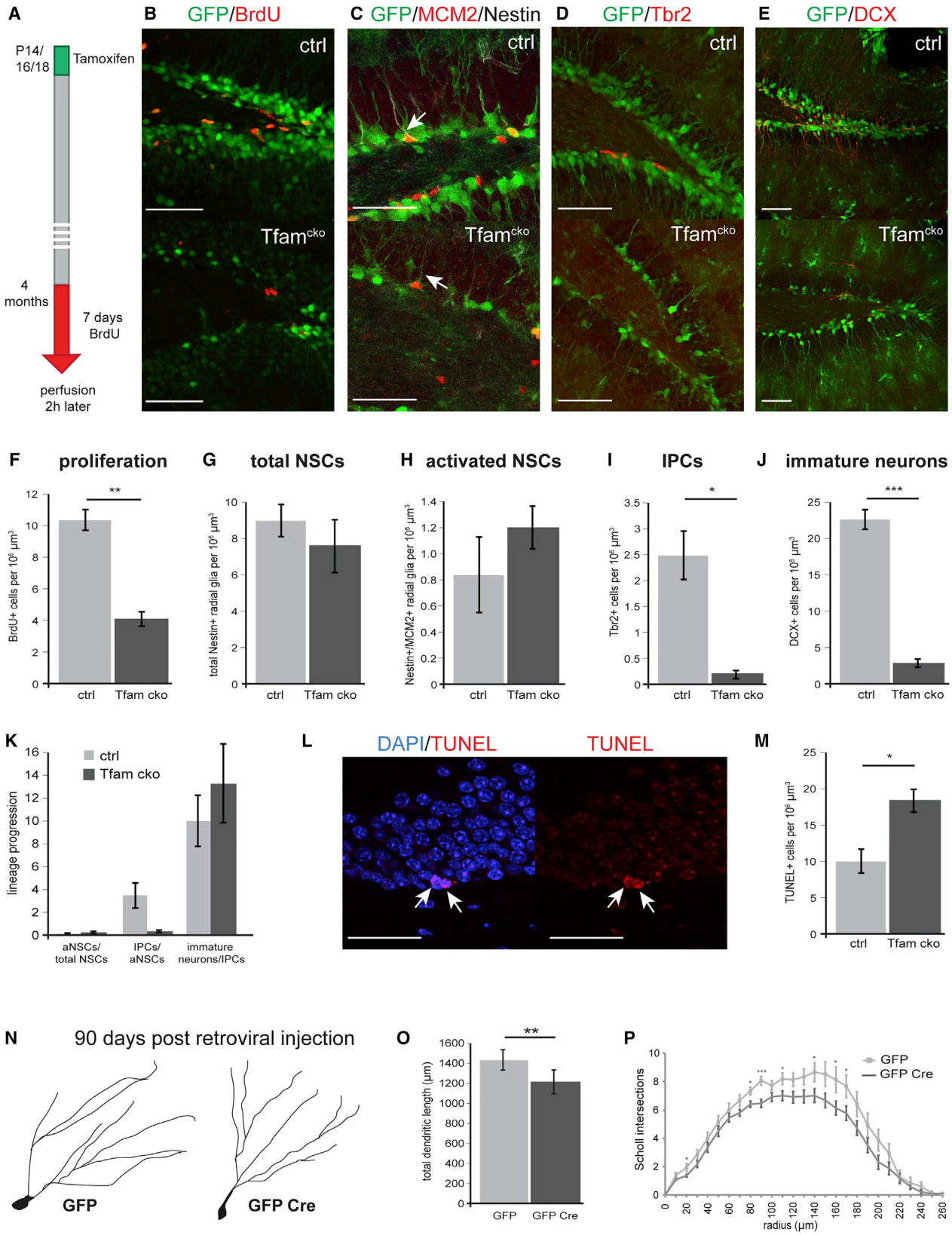

(legend on next page)

severely decreased in *Tfam*^{cko} mice. To better estimate transitions between developmental stages, we calculated a lineage progression index by dividing the number of cells of a defined developmental stage by the number of cells of the preceding developmental stage. Comparison of the lineage progression index between control and *Tfam*^{cko} mice (Figure 3K) demonstrated that *Tfam* depletion produced a severe defect in the neurogenic lineage at the level of IPCs, which is consistent with the transcriptome-based prediction of mt complex dependency around the time of transition from activated NSCs and IPCs (Figures 1H–1J).

Terminal deoxynucleotidyl transferase dUTP nick end labeling (TUNEL) analysis revealed a significantly increased number of apoptotic cells in the DG of 4-month-old *Tfam*^{cko} mice (Figures 3L and 3M). Attempts to phenotype apoptotic cells by immunohistochemistry were unsuccessful, most likely because of the loss of cellular integrity and gene expression of apoptotic cells. However, our findings that *Tfam* deletion results in strongly impaired viability of cultured NSPCs (Figure 2I) and that BMP4-induced quiescence resulted in a trend toward higher viability of *Tfam*-deficient NSPCs ($p = 0.066$) (Figure S2G) suggests that the increase in apoptotic cells was caused in part by programmed cell death of proliferating progenitors.

We also investigated whether mitochondrial dysfunction induced by *Tfam* deletion impeded later developmental stages, in particular, neuronal growth. To this end, *Tfam*$^{loxP/loxP}$ mice were stereotaxically injected with a recombinant MMLV bi-cistronically encoding for GFP and Cre-recombinase to induce *Tfam* deletion starting around the stage of IPCs and neuroblasts (Tashiro et al., 2006). *Tfam*$^{loxP/loxP}$ mice injected with an MMLV encoding for GFP served as controls. *Tfam*-ablated neurons displayed mildly shortened dendritic length and decreased dendritic complexity at 90 days post-viral injection (Figures 3N–3P). These observations indicate that impairment of the ETC or oxPhos machinery compromised growth and maturation of adult-born neurons, which lends support to the recent suggestion that precise regulation of mitochondrial metabolism is required for the morphological and functional development of adult-born neurons (Oruganty-Das et al., 2012; Steib et al., 2014).

Mitochondrial dysfunction is postulated to contribute to organismal aging (López-Otín et al., 2013); its impact on age-associated impairment of hippocampal neurogenesis, however, remains undetermined. Analysis of young (4-month-old) and middle-aged (1-year-old) mice confirmed the previously described age-associated neurogenesis deficit (Drapeau and Nora Abrous, 2008): thus, middle-aged mice revealed a severe cell proliferation deficit (Figures S4A, S4B, and S4D) and showed a pronounced (i.e., up to 10-fold) decrease in the number of radial glia-like NSCs, activated NSCs, IPCs, and DCX$^+$ neuroblasts and immature neurons (Figures S4C and S4E–S4H).

To extend the insight into how aging impacts on the adult neurogenic lineage and on the transition between developmental stages, we calculated the lineage progression index (Figure 4A). The proportion of activated NSCs among NSCs was comparable between young and middle-aged animals. In contrast, the ratio of IPCs to activated NSCs was greatly reduced in older animals (Figure 4A), suggesting that aging impedes on neurogenic lineage progression at the level of generation of the highly proliferative IPC population. In line with a recent report (Seib et al., 2013), immature DCX$^+$ neurons in older mice bore only short processes that mostly terminated at the border between granule cell layer and molecular layer (Figure S4C). To extend the knowledge on the impact of aging on dendritic development, we compared the morphology of mature (i.e., 2-month-old) neurons generated in young and middle-aged mice using an MMLV encoding for GFP. As a consequence of the age-dependent decrease in proliferation activity, we were unable to efficiently label adult-born neurons in 1-year-old animals. We therefore opted to visualize DG neurons generated in 8-month-old mice and to compare their morphology to their counterparts generated in 2-month-old mice. Neurons generated in older mice bore a shorter and less complex dendritic tree compared to neurons generated in young animals (Figures 4B–4D), indicating that aging impacts on dendritic growth and results in a persistent dendritic morphology deficit.

The similarities between age-dependent alterations of the NSC lineage and the *Tfam*^{cko} mice phenotype (i.e., proliferation deficit, decreased generation of new neurons, lineage progression deficit at the transition from activated NSCs to IPCs, but not the loss of radial glia-like NSCs), prompted us to search for evidence of age-associated mitochondrial dysfunction in the adult hippocampal neurogenic lineage. All radial glia-like NSCs and IPCs in young mice (4 months) and middle-aged mice (1 year) contained Cox$^+$ mitochondria. Intriguingly, HSP60-based morphological evaluation of mitochondria revealed that in contrast to radial glia-like NSCs in 4-month-old mice (Figure 4E), around one-third (34%) of the NSC population in 1-year-old mice harbored

Figure 3. *Tfam* Deficiency Does Not Affect NSCs but Impairs Neurogenesis at the Level of IPCs in 4-Month-Old Mice

(A) Experimental scheme of BrdU-paradigm used in (B and F).

(B and F) Confocal images and quantification of control and *Tfam*^{cko} mice showed a significant reduction in the number BrdU-expressing cells (red). GFP-reporter$^+$ cells are shown in green.

(C–J) (C and G) Confocal images and quantification of Nestin immunoreactive cells (white) indicated no differences in number of total NCSs between control and *Tfam*^{cko} mice; (C and H) activation of NSCs was not affected as revealed by quantification of cells co-expressing Nestin and the cell-cycle marker MCM2 (red, arrow). Tbr2$^+$ IPCs (red; D) as well as DCX$^+$ immature neurons (red; E) were significantly reduced in *Tfam*^{cko} mice (I and J).

(K) Comparison of the lineage progression index between ctrl and *Tfam*^{cko} mice reveals impaired generation of IPCs. The lineage progression index is calculated by dividing the number of cells of a defined developmental stage by the number of cells of the preceding developmental stage (aNSCs normalized to total NSCs, IPCs normalized to aNSCs, immature neurons normalized to IPCs). Index aNSCs/total NSCs: ctrl = 0.1, *Tfam*^{cko} = 0.14; index IPCs/aNSCs: *Tfam*^{cko} = 0.23.

(L and M) Confocal images of TUNEL$^+$ cells in *Tfam*^{cko} mice (red; arrow); quantification of TUNEL$^+$ cells revealed a significant increase in apoptosis upon deletion of *Tfam* (M).

(N–P) Morphological analysis of newborn neurons in *Tfam*$^{fl/fl}$ mice 90 days post injection with MMLV vectors encoding for GFP alone (GFP) or for GFP and Cre (GFP Cre) revealed impaired dendritic morphology upon *Tfam* deletion. (F, G, I, and J) $n_{ctrl} = 3$, $n_{cko} = 4$; (H) $n_{ctrl} = 3$, $n_{cko} = 3$; (M) $n_{ctrl} = 4$, $n_{cko} = 5$; (O and P) $n_{GFP} = 16$ cells, $n_{GFP\ Cre} = 20$ cells (Table S1). Data represented as mean ± SEM; t test was performed to determine significance; all scale bars = 20 μm.

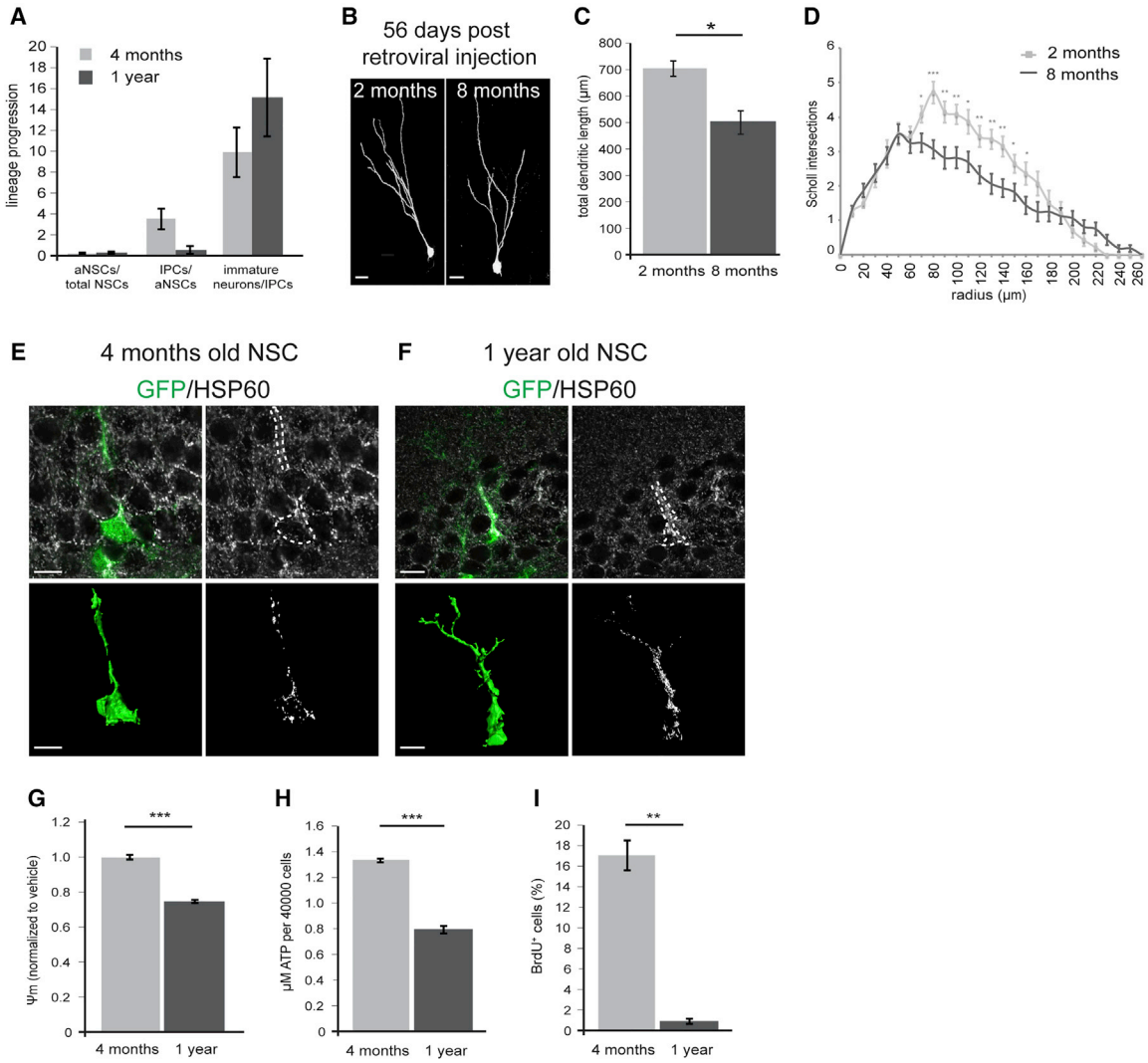

Figure 4. *Tfam* Deletion Reproduces Multiple Aspects of Aging in Hippocampal Neurogenesis

(A) Comparison of the lineage progression index between young (4-month-old) and middle-aged (1-year-old) mice. Index aNSCs/total NSCs: 4 months = 0.1, 1 year = 0.15; index IPCs/aNSCs: 1 year = 0.52.

(B) Representative confocal images of MMLV-birthdated mature (56 dpi) DG neurons generated in 2- and 8-month-old wild-type mice.

(C and D) Neurons generated in 8-month-old wild-type mice display impaired dendritic morphology as evidenced by shorter total dendritic length (C) and less intersections in Scholl-analysis (D).

(E and F) Comparison of mitochondria in NSCs of young and middle-aged mice, visualized by immunostaining against HSP60 (white); NSCs are identified by GFP expression (green) and radial morphology in the *hGFAPeGFP* mouse line; bottom panels are reconstructions for GFP (green; bottom left) and HSP60 (white; bottom right). Upon aging, mitochondria increase in number and had a clumped appearance.

(G–I) Membrane potential (G), ATP content (H), and proliferation (I) are significantly decreased in NSPCs isolated from 1-year-old mice compared to NSPCs derived from 4-month-old mice. (C and D) $n_{2\ months}$ = 14 cells, $n_{8\ months}$ = 16 cells (Table S1). Data presented as mean ± SEM; t test was performed to determine significance; scale bars = 10 µm.

densely packed mitochondria of clumpy appearance in their radial process (Figure 4F). IPCs in 1-year-old mice did not display obvious alterations in mitochondrial morphology (Figures S4I and S4J); the elongated morphology of mitochondria in IPCs (Figure 1B), however, may have masked alterations in mitochondrial morphology such as mitochondrial clumping.

Next, we sought to compare mitochondrial function NSPCs from young and middle-aged mice. Notably, we were unable to consistently establish NSPC cultures from the dissected hippocampus of 1-year-old mice, most likely because of the age-associated low number and impaired proliferative capacity of NSPCs in the hippocampal neurogenic niche. In analogy to hippocampal neurogenesis, neurogenic activity in the main neurogenic niche of the rodent forebrain, i.e., the subependymal zone (SEZ) of the lateral ventricles, is greatly impaired during aging (Shook et al., 2012). Compared to the hippocampal DG, the SEZ harbors

greater numbers of NSPCs and thus allowed us to establish NSPC cultures from 1-year-old mice to investigate age-associated alterations to mitochondrial function in NSPCs. In line with a recent report of age-associated defective oxidative metabolism in forebrain-derived NSPCs (Perry et al., 2011; Stoll et al., 2011), we found that age-dependent proliferation deficits were accompanied by decreased mitochondrial membrane potential and lower levels of ATP (Figures 4G–4I).

Collectively, these findings suggested that mitochondrial dysfunction contributes to diminished hippocampal neurogenesis during aging and raised the intriguing possibility that enhancement of mitochondrial function may improve neurogenesis during aging. The nootropic compound piracetam is used for the treatment of age-related cognitive impairment and dementia (Waegemans et al., 2002) and was found to enhance—among other mitochondrial parameters—mitochondrial respiration, ETC activity, and ATP production in particular in cells with compromised mitochondrial function (Costa et al., 2013; Keil et al., 2006; Kurz et al., 2010; Leuner et al., 2010; Stockburger et al., 2013; Zhang et al., 2010). Piracetam treatment of NSPCs derived from 1-year-old mice resulted in a trend toward increased proliferation, which was paralleled by a significant increase in ATP production in the absence of changes in mitochondrial membrane potential (Figures 5A–5C). To investigate whether piracetam-induced enhancement of NSPC proliferation depended on the integrity of the ETC and/or oxPhos machinery, we first analyzed the effects of piracetam on *Tfam*-deficient NSPCs. While piracetam treatment did not alter ATP production, it surprisingly increased mitochondrial membrane potential (Figures S5A and S5B), suggesting that *Tfam*-deficient NSPCs harbored residual function of mitochondrial complexes, which could be enhanced by piracetam treatment. Interestingly, we also observed a piracetam-induced increase in proliferation of *Tfam*-deficient GFP-reporter$^+$ NSPCs (Figure S5C). Because these results did not provide unequivocal insight into the requirement of a functional ETC and oxPhos machinery for piracetam-induced enhancement of proliferation, we tested the effects of piracetam in the context of rotenone- and oligomycin-induced inhibition of the ETC and oxPhos machinery. Treatment with piracetam neither increased mitochondrial membrane potential nor ATP production (Figures S5D–S5F). Most importantly, piracetam did not ameliorate the proliferation defect of rotenone- and oligomycin-treated cultures as evidenced by the complete absence of BrdU incorporating NSPCs, suggesting that piracetam-induced enhancement of NSPC proliferation is dependent on the amelioration of mitochondrial dysfunction and requires residual ETC and oxPhos activity.

Finally, we investigated piracetam's potential to ameliorate age-associated hippocampal neurogenesis defects. To this end, 18-month-old mice received a daily oral dose of piracetam for 14 days; control mice received a corresponding dose of the solvent. Animals were perfused 1 day after the last dose (Figure 5D). Immunostainings of the DG using HSP60 and an antibody cocktail that recognizes components of mt complexes I-V showed that piracetam treatment resulted in a more homogeneous expression of mt complexes I-V in HSP60$^+$ mitochondria. Moreover, we occasionally observed in untreated animals radial glia-like GFAP$^+$ cells that contained mitochondria with an aberrant clumpy morphology, which appeared to be less frequent in piracetam-treated animals (Figure 5E). Consistent with the age-dependent neurogenesis impairment, 18-month-old control animals had very low numbers of MCM2$^+$ proliferating cells, Nestin$^+$/MCM2$^+$ activated NSCs, Tbr2$^+$ IPCs, and DCX$^+$ immature neurons (Figures 5F–5K). Piracetam treatment did not alter radial glia-like NSC numbers (data not shown). The number of proliferating cells, however, was approximately doubled upon piracetam treatment ($p = 0.07$; Figures 5F and 5H). The number of IPCs and of DCX$^+$ immature neurons was significantly higher in piracetam-treated animals and there was a trend toward increased number of activated NSCs following piracetam treatment ($p = 0.19$; Figures 5G and 5I–5K). Lineage progression analysis indicated that piracetam treatment stimulated neurogenesis on the level of IPCs and also suggested the possibility that piracetam enhanced the generation of activated stem cells (Figure 5L). Moreover, we observed that DCX$^+$ neurons in piracetam-treated mice displayed a higher total dendritic length and a more complex dendritic morphology (Figures 5M–5O) and extended dendrites deep into molecular cell layer similar to newborn neurons in the young brain (Figure 5G). These results demonstrate that piracetam improved age-associated hippocampal neurogenesis defects. It is, however, important to point out that piracetam did not restore neurogenesis to levels observed in young mice (compare Figures 3J and 5K for numbers of DCX$^+$ newborn neurons), which may reflect the multifactorial cause of age-associated neurogenesis defects as well as the pronounced depletion of radial glia-like NSCs in the hippocampus of aged mice.

DISCUSSION

Here, we provide in vivo functional genetic evidence supported by gene expression profiling that the adult hippocampal neurogenic lineage is critically dependent on mitochondrial complex function at the level of IPCs. Thus, our data strongly support the emerging notion that stage-specific metabolic programs are functionally linked to distinct developmental steps within the NSC lineage (Beckervordersandforth et al., 2015; Folmes et al., 2012; Knobloch and Jessberger, 2015; Rafalski and Brunet, 2011; Yeo et al., 2013).

Recent reports indicated that highly proliferating embryonic neural stem and progenitor cells are glycolytic and that high oxPhos activity is associated with termination of proliferation and neuronal differentiation (Agathocleous et al., 2012; Homem et al., 2014; Khacho et al., 2016; Zheng et al., 2016). Thus, our finding that mitochondrial complex function is already required in the highly proliferative IPC population was unexpected. Very recent in vitro studies indicated that cancer cells require ETC function to regenerate electron acceptors for the biosynthesis of the limiting amino acid aspartate in order to sustain high levels of proliferation (Birsoy et al., 2015; Sullivan et al., 2015). Another intriguing possibility would be that mitochondrial complexes are required to generate reactive oxygen species, which have recently been described to regulate embryonic NSPC proliferation (Forsberg et al., 2013; Hou et al., 2012; Khacho et al., 2016). It will be interesting to determine whether IPCs require only a functional ETC or both ETC and oxPhos activity and which

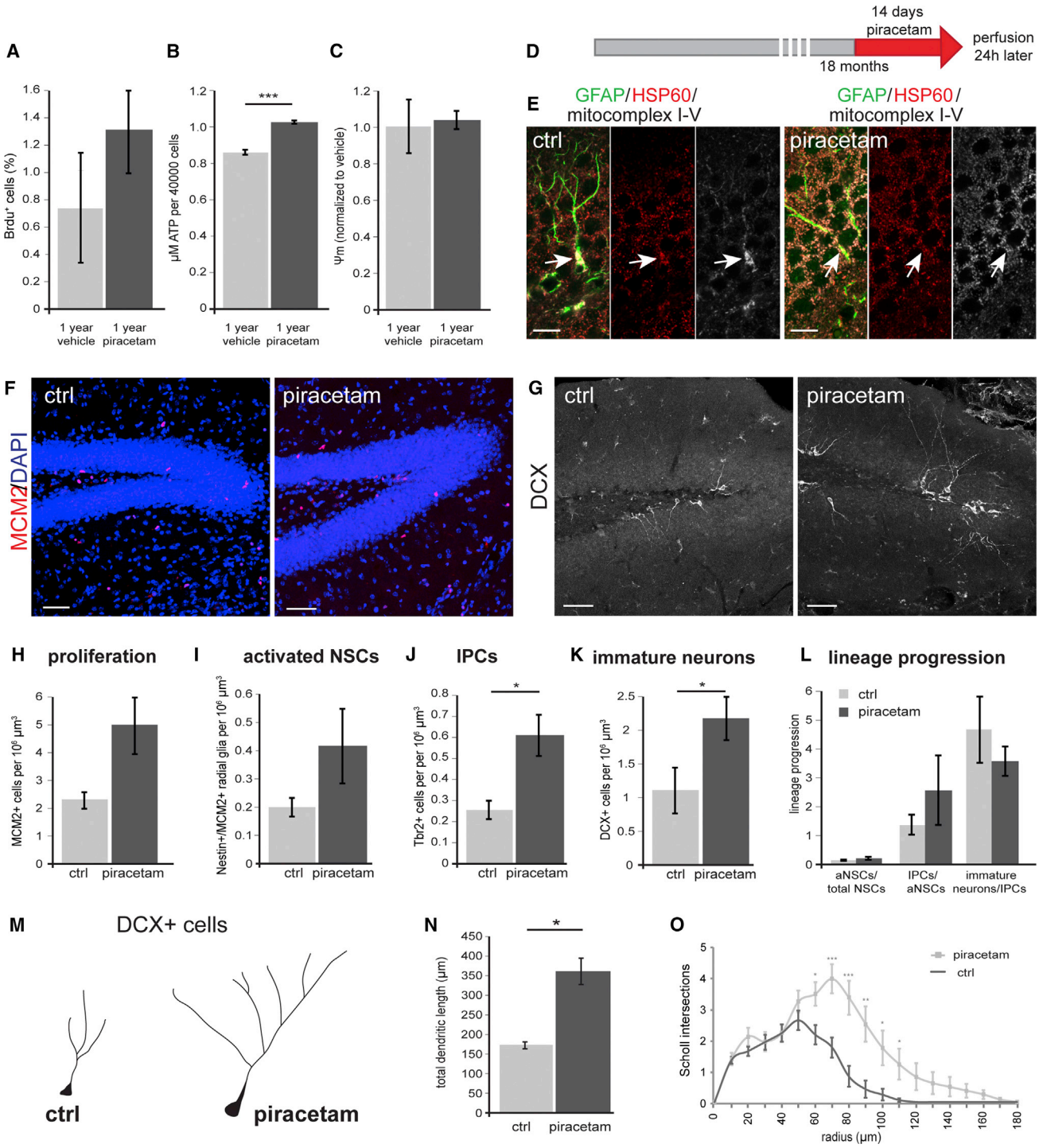

Figure 5. Administration of Piracetam Ameliorates Aging-Associated Defects in Hippocampal Neurogenesis

(A–C) Treatment of NSPCs derived from 1-year-old mice with piracetam resulted in a trend toward increased proliferation (A). Piracetam significantly increased ATP production in NSPCs (B) but did not change membrane potential (C).

(D) Experimental scheme of Piracetam administration to 18-month-old wild-type mice.

(E) Radial-glia like GFAP$^+$ cells (green) in untreated animals occasionally revealed mitochondria of clumpy appearance (arrow) combined with increased immunoreactivity of HSP60 (red) and mitochondrial complexes I-V (white). Upon piracetam treatment this mitochondrial phenotype was less frequent (arrow).

(F and G) Representative confocal images of MCM2$^+$ (F; red) and DCX$^+$ cells (G; white) in control (ctrl) and Piracetam-treated mice.

(H–K) Piracetam-treated mice show increased numbers of MCM2$^+$ proliferating cells, activated NSCs, IPCs, and DCX$^+$ neurons.

(legend continued on next page)

essential metabolic circuits and developmental processes are enabled by ETC or oxPhos activity in the early adult neurogenic lineage.

Genetic ablation of ETC and oxPhos activity via deletion of *Tfam* in the adult hippocampal neurogenic lineage resulted in a profound loss of IPCs. The massively increased cell death of NSPCs with impaired ETC and oxPhos activity as well as the increased appearance of apoptotic cells in the hippocampal neurogenic niche of $Tfam^{cko}$ mice strongly suggests that impaired ETC and oxPhos activity are critical for viability of IPCs. It is, however, possible that block of lineage progression of activated stem cells and/or decreased proliferation of IPCs also significantly contributed to the $Tfam^{cko}$ in vivo phenotype.

An important consideration when interpreting the results is the fact that *Tfam* was also deleted from astrocytes when using *GLAST-CreER*^{T2}. We cannot fully exclude that *Tfam* deficiency in astrocytes partially contributed to the neurogenesis phenotype. However, consistent with the view that astrocytes are predominantly glycolytic and do not require oxPhos (Bélanger et al., 2011), astrocyte numbers and morphology in the hippocampal neurogenic niche were unchanged in $Tfam^{cko}$ mice (Figure S3). Moreover, in vitro analysis demonstrated that Tfam deficiency directly affected proliferation and survival in NSPC cultures, which are largely devoid of astrocytes. We would therefore argue that the neurogenesis defects in $Tfam^{cko}$ mice are to a significant extent the result of *Tfam* deficiency in the neurogenic lineage. Nevertheless, the specific impact of astrocytic *Tfam* deletion on neurogenesis should be investigated in the future.

Decreased hippocampal neurogenesis is a common hallmark of mammalian aging (Kempermann et al., 1998; Kuhn et al., 1996; Spalding et al., 2013). It has been suggested that the neurogenesis phenotype during aging is caused by a combination of systemic and cell-intrinsic aging factors (Katsimpardi et al., 2014; Molofsky et al., 2006; Smith et al., 2015). The precise mechanisms and the identity of contributing factors underlying the age-associated impairment in hippocampal neurogenesis remain, however, largely unknown. Mitochondrial dysfunction was previously proposed as a major contributing factor to age-associated neurogenesis deficits (Ahlqvist et al., 2012; Cheng et al., 2010; Stoll et al., 2011, 2015). Such connection remained speculative, as published animal models for mitochondrial dysfunction failed to reproduce the severe proliferation and neurogenesis defects found during aging (Ahlqvist et al., 2012). Our findings that *Tfam* ablation in NSCs phenocopies key aspects of aging, that aging is associated with altered mitochondrial load and the appearance of morphologically abnormal mitochondria in radial glia-like NSCs, and that pharmacological enhancement of mitochondrial function promotes hippocampal neurogenesis in aged animals provide evidence for mitochondrial dysfunction as a key contributor to age-associated impairment of hippocampal neurogenesis.

Aging is also a major negative regulator of neurogenic activity in the SEZ of the lateral ventricles (Shook et al., 2012). It will be important to establish to which extent the neurogenic lineages of the SEZ/olfactory bulb system and of the hippocampus are controlled by overlapping metabolic programs and whether impaired metabolism contributes to aging phenotypes in the SEZ. The findings that NSPCs derived from forebrain of middle-aged rodents display profound mitochondrial dysfunction (Stoll et al., 2011 and this study) and that genetically induced enhancement of mitochondrial biogenesis promotes generation of new neurons in the SEZ of aged mice (Stoll et al., 2015), however, suggest that mitochondrial dysfunction is also a significant contributor to age-associated impairment of neurogenesis in the SEZ/olfactory bulb system.

We found short-term piracetam treatment of aged animals to be sufficient to promote neurogenesis, suggesting mitochondrial metabolism as a potential pharmacological target to ameliorate age-associated hippocampal neurogenesis deficits. Lineage progression analysis suggested that piracetam may enhance neurogenesis already at the stage of stem cell activation. This observation appears to contradict the notion that ETC and oxPhos function are critical at the stage of IPCs. Piracetam improves different sets of mitochondrial parameters in compromised cells depending on the experimental context (Figures 5A–5C and S5; Costa et al., 2013; Keil et al., 2006; Kurz et al., 2010; Leuner et al., 2010; Stockburger et al., 2013; Zhang et al., 2010), suggesting that piracetam impacts on a number of pathways in mitochondria. As the function of metabolic pathways in stem cell and neurogenesis regulation is only beginning to unfold, one cannot exclude the possibility that piracetam promoted NSC activation through a critical mitochondrial pathway other than ETC or oxPhos. The systemic administration of piracetam may have also affected the function of neurogenic niche cells, which are providing key regulatory signals in hippocampal neurogenesis (Aimone et al., 2014). Supporting this notion are our observations that piracetam resulted in a more homogeneous expression of mitochondrial complexes throughout the DG and that piracetam had a more robust effect on proliferation in vivo than on proliferation in vitro. A detailed understanding of the critical mitochondrial metabolic circuits in adult neurogenesis and of the impact of aging on mitochondrial dysfunction in the neurogenic lineage and the neurogenic niche could support the development of novel strategies to ameliorate neurogenesis-dependent cognitive deficits in aging.

STAR★METHODS

Detailed methods are provided in the online version of this paper and include the following:

- KEY RESOURCES TABLE
- CONTACT FOR REAGENT AND RESOURCE SHARING
- EXPERIMENTAL MODEL AND SUBJECT DETAILS
- METHOD DETAILS
  - Tissue processing

(L) Lineage progression analysis of control and Piracetam-treated aged mice. Index aNSCs/total NSCs: control = 0.02, piracetam = 0.04.
(M–O) DCX$^+$ neurons display a more complex morphology upon Piracetam treatment with longer (N) and more elaborate processes (O). (H–J) $n_{ctrl} = 5$, $n_{piracetam} = 5$; (K) $n_{ctrl} = 5$, $n_{piracetam} = 4$; (N and O) $n_{ctrl} = 18$ cells, $n_{piracetam} = 26$ cells (Table S1). Data represented as mean ± SEM; t test was performed to determine significance; scale bars = 10 μm (E) and 20 μm (F and G).

- Tfam genotyping
- EM processing
- In vitro assays
- Histology and counting procedures
- Cell death analysis
- BrdU administration
- Piracetam administration
- Retrovirus preparation and stereotactic injections

- QUANTIFICATION AND STATISTICAL ANALYSIS
  - EM mitochondrial volume analyses
  - Analysis of transcriptomic resource
  - Expression analysis of stage-specific markers
  - Dendritic morphology analyses
  - Statistical analysis
- DATA AND SOFTWARE AVAILABLILTY

SUPPLEMENTAL INFORMATION

Supplemental Information includes five figures, one table, and three movies and can be found with this article online at http://dx.doi.org/10.1016/j.neuron.2016.12.017.

AUTHOR CONTRIBUTIONS

Conceptualization, R.B., B.E., R.J., and D.C.L.; Investigation, R.B., B.E., I.S., J.M., C.F., J.S., D.L.M., L.G., M.F.T., C.S., K.S., J.v.W., S.K., W.X., and S.M.H.; Formal analysis, B.E., R.B., I.S., J.S., J.M., D.L.M., L.G., M.F.T., and D.C.L.; Resources and Funding acquisition, K.F., C.R., W.W., A.F.S., S.J., G.M., H.S., N.T., and D.C.L.; Writing-Original draft, R.B., D.C.L.; Writing-Review and Editing, R.B., S.J., H.J., and D.C.L.; Supervision: C.R., K.L., A.F.S., S.J., G.M., H.S., N.T., and D.C.L.

ACKNOWLEDGMENTS

We thank M. Götz (LMU Munich) and N. Larsson (Max Planck Institute for Biology of Ageing, Cologne) for providing the GLAST::CreERT2 and the Tfam-loxP/loxP mice, respectively. K.S. was supported by a fellowship of the Schering foundation. This work was supported by grants from the German Research Foundation (DFG; BE 5136/1-1 to R.B., LI 858/6-3 and 9-1 to D.C.L., INST 410/45-1 FUGG), the Bavarian Research Network "ForIPS," the Helmholtz Alliance for Mental Health in an Ageing Society, the University Hospital Erlangen (IZKF grants E12, E16, and E21 to D.C.L., E11 to W.X.), the NIH (R37NS047344 and P01 NS097206 to H.S, and R35NS097370 and R01MH105128 to G.M.), and the Swiss National Science Foundation (SNSF 31003A-156943 to S.J. and PPOOA-119026/1 to N.T.). C.F. and R.B. are members of the research training group 2162 "Neurodevelopment and Vulnerability of the Central Nervous System" of the Deutsche Forschungsgemeinschaft (DFG GRK2162/1).

Received: August 20, 2015
Revised: August 6, 2016
Accepted: November 23, 2016
Published: January 19, 2017; corrected online March 14, 2017

REFERENCES

Abrous, D.N., and Wojtowicz, J.M. (2015). Interaction between Neurogenesis and Hippocampal Memory System: New Vistas. Cold Spring Harb. Perspect. Biol. *7*, 7.

Agathocleous, M., Love, N.K., Randlett, O., Harris, J.J., Liu, J., Murray, A.J., and Harris, W.A. (2012). Metabolic differentiation in the embryonic retina. Nat. Cell Biol. *14*, 859–864.

Ahlqvist, K.J., Hämäläinen, R.H., Yatsuga, S., Uutela, M., Terzioglu, M., Götz, A., Forsström, S., Salven, P., Angers-Loustau, A., Kopra, O.H., et al. (2012). Somatic progenitor cell vulnerability to mitochondrial DNA mutagenesis underlies progeroid phenotypes in Polg mutator mice. Cell Metab. *15*, 100–109.

Aimone, J.B., Li, Y., Lee, S.W., Clemenson, G.D., Deng, W., and Gage, F.H. (2014). Regulation and function of adult neurogenesis: from genes to cognition. Physiol. Rev. *94*, 991–1026.

Alirol, E., and Martinou, J.C. (2006). Mitochondria and cancer: is there a morphological connection? Oncogene *25*, 4706–4716.

Alle, H., Roth, A., and Geiger, J.R. (2009). Energy-efficient action potentials in hippocampal mossy fibers. Science *325*, 1405–1408.

Attwell, D., and Laughlin, S.B. (2001). An energy budget for signaling in the grey matter of the brain. J. Cereb. Blood Flow Metab. *21*, 1133–1145.

Beckervordersandforth, R., Häberle, B.M., and Lie, D.C. (2015). Metabolic regulation of adult stem cell-derived neurons. Front. Biol. *10*, 107–116.

Bélanger, M., Allaman, I., and Magistretti, P.J. (2011). Brain energy metabolism: focus on astrocyte-neuron metabolic cooperation. Cell Metab. *14*, 724–738.

Birsoy, K., Wang, T., Chen, W.W., Freinkman, E., Abu-Remaileh, M., and Sabatini, D.M. (2015). An essential role of the mitochondrial electron transport chain in cell proliferation is to enable aspartate synthesis. Cell *162*, 540–551.

Bond, A.M., Ming, G.L., and Song, H. (2015). Adult mammalian neural stem cells and neurogenesis: five decades later. Cell Stem Cell *17*, 385–395.

Cheng, A., Hou, Y., and Mattson, M.P. (2010). Mitochondria and neuroplasticity. ASN Neuro *2*, e00045.

Christian, K.M., Song, H., and Ming, G.L. (2014). Functions and dysfunctions of adult hippocampal neurogenesis. Annu. Rev. Neurosci. *37*, 243–262.

Costa, R.A., Fernandes, M.P., de Souza-Pinto, N.C., and Vercesi, A.E. (2013). Protective effects of l-carnitine and piracetam against mitochondrial permeability transition and PC3 cell necrosis induced by simvastatin. Eur. J. Pharmacol. *701*, 82–86.

Drapeau, E., and Nora Abrous, D. (2008). Stem cell review series: role of neurogenesis in age-related memory disorders. Aging Cell *7*, 569–589.

Ekstrand, M.I., Terzioglu, M., Galter, D., Zhu, S., Hofstetter, C., Lindqvist, E., Thams, S., Bergstrand, A., Hansson, F.S., Trifunovic, A., et al. (2007). Progressive parkinsonism in mice with respiratory-chain-deficient dopamine neurons. Proc. Natl. Acad. Sci. USA *104*, 1325–1330.

Eriksson, P.S., Perfilieva, E., Björk-Eriksson, T., Alborn, A.M., Nordborg, C., Peterson, D.A., and Gage, F.H. (1998). Neurogenesis in the adult human hippocampus. Nat. Med. *4*, 1313–1317.

Fiala, J.C. (2005). Reconstruct: a free editor for serial section microscopy. J. Microsc. *218*, 52–61.

Folmes, C.D., Dzeja, P.P., Nelson, T.J., and Terzic, A. (2012). Metabolic plasticity in stem cell homeostasis and differentiation. Cell Stem Cell *11*, 596–606.

Forsberg, K., Wuttke, A., Quadrato, G., Chumakov, P.M., Wizenmann, A., and Di Giovanni, S. (2013). The tumor suppressor p53 fine-tunes reactive oxygen species levels and neurogenesis via PI3 kinase signaling. J. Neurosci. *33*, 14318–14330.

Hall, C.N., Klein-Flügge, M.C., Howarth, C., and Attwell, D. (2012). Oxidative phosphorylation, not glycolysis, powers presynaptic and postsynaptic mechanisms underlying brain information processing. J. Neurosci. *32*, 8940–8951.

Hamberger, A., and Hyden, H. (1963). Inverse enzymatic changes in neurons and glia during increased function and hypoxia. J. Cell Biol. *16*, 521–525.

Hodge, R.D., Nelson, B.R., Kahoud, R.J., Yang, R., Mussar, K.E., Reiner, S.L., and Hevner, R.F. (2012). Tbr2 is essential for hippocampal lineage progression from neural stem cells to intermediate progenitors and neurons. J. Neurosci. *32*, 6275–6287.

Homem, C.C., Steinmann, V., Burkard, T.R., Jais, A., Esterbauer, H., and Knoblich, J.A. (2014). Ecdysone and mediator change energy metabolism to terminate proliferation in Drosophila neural stem cells. Cell *158*, 874–888.

Hou, Y., Ouyang, X., Wan, R., Cheng, H., Mattson, M.P., and Cheng, A. (2012). Mitochondrial superoxide production negatively regulates neural progenitor proliferation and cerebral cortical development. Stem Cells *30*, 2535–2547.

Hyden, H., and Lange, P.W. (1962). A kinetic study of the neuronglia relationship. J. Cell Biol. *13*, 233–237.

Katsimpardi, L., Litterman, N.K., Schein, P.A., Miller, C.M., Loffredo, F.S., Wojtkiewicz, G.R., Chen, J.W., Lee, R.T., Wagers, A.J., and Rubin, L.L. (2014). Vascular and neurogenic rejuvenation of the aging mouse brain by young systemic factors. Science *344*, 630–634.

Keil, U., Scherping, I., Hauptmann, S., Schuessel, K., Eckert, A., and Müller, W.E. (2006). Piracetam improves mitochondrial dysfunction following oxidative stress. Br. J. Pharmacol. *147*, 199–208.

Kempermann, G., Kuhn, H.G., and Gage, F.H. (1998). Experience-induced neurogenesis in the senescent dentate gyrus. J. Neurosci. *18*, 3206–3212.

Khacho, M., Clark, A., Svoboda, D.S., Azzi, J., MacLaurin, J.G., Meghaizel, C., Sesaki, H., Lagace, D.C., Germain, M., Harper, M.E., et al. (2016). Mitochondrial Dynamics Impacts Stem Cell Identity and Fate Decisions by Regulating a Nuclear Transcriptional Program. Cell Stem Cell *19*, 232–247.

Knobloch, M., and Jessberger, S. (2015). Metabolic control of adult neural stem cell behavior. Front. Biol. *10*, 100–106.

Knobloch, M., Braun, S.M., Zurkirchen, L., von Schoultz, C., Zamboni, N., Araúzo-Bravo, M.J., Kovacs, W.J., Karalay, O., Suter, U., Machado, R.A., et al. (2013). Metabolic control of adult neural stem cell activity by Fasn-dependent lipogenesis. Nature *493*, 226–230.

Kuhn, H.G., Dickinson-Anson, H., and Gage, F.H. (1996). Neurogenesis in the dentate gyrus of the adult rat: age-related decrease of neuronal progenitor proliferation. J. Neurosci. *16*, 2027–2033.

Kurz, C., Ungerer, I., Lipka, U., Kirr, S., Schütt, T., Eckert, A., Leuner, K., and Müller, W.E. (2010). The metabolic enhancer piracetam ameliorates the impairment of mitochondrial function and neurite outgrowth induced by beta-amyloid peptide. Br. J. Pharmacol. *160*, 246–257.

Larsson, N.G., Wang, J., Wilhelmsson, H., Oldfors, A., Rustin, P., Lewandoski, M., Barsh, G.S., and Clayton, D.A. (1998). Mitochondrial transcription factor A is necessary for mtDNA maintenance and embryogenesis in mice. Nat. Genet. *18*, 231–236.

Leuner, K., Kurz, C., Guidetti, G., Orgogozo, J.M., and Müller, W.E. (2010). Improved mitochondrial function in brain aging and Alzheimer disease - the new mechanism of action of the old metabolic enhancer piracetam. Front. Neurosci. *4*, 44.

Lie, D.C., Dziewczapolski, G., Willhoite, A.R., Kaspar, B.K., Shults, C.W., and Gage, F.H. (2002). The adult substantia nigra contains progenitor cells with neurogenic potential. J. Neurosci. *22*, 6639–6649.

López-Otín, C., Blasco, M.A., Partridge, L., Serrano, M., and Kroemer, G. (2013). The hallmarks of aging. Cell *153*, 1194–1217.

Lugert, S., Basak, O., Knuckles, P., Haussler, U., Fabel, K., Götz, M., Haas, C.A., Kempermann, G., Taylor, V., and Giachino, C. (2010). Quiescent and active hippocampal neural stem cells with distinct morphologies respond selectively to physiological and pathological stimuli and aging. Cell Stem Cell *6*, 445–456.

Martynoga, B., Mateo, J.L., Zhou, B., Andersen, J., Achimastou, A., Urbán, N., van den Berg, D., Georgopoulou, D., Hadjur, S., Wittbrodt, J., et al. (2013). Epigenomic enhancer annotation reveals a key role for NFIX in neural stem cell quiescence. Genes Dev. *27*, 1769–1786.

Mira, H., Andreu, Z., Suh, H., Lie, D.C., Jessberger, S., Consiglio, A., San Emeterio, J., Hortigüela, R., Marqués-Torrejón, M.A., Nakashima, K., et al. (2010). Signaling through BMPR-IA regulates quiescence and long-term activity of neural stem cells in the adult hippocampus. Cell Stem Cell *7*, 78–89.

Molofsky, A.V., Slutsky, S.G., Joseph, N.M., He, S., Pardal, R., Krishnamurthy, J., Sharpless, N.E., and Morrison, S.J. (2006). Increasing p16INK4a expression decreases forebrain progenitors and neurogenesis during ageing. Nature *443*, 448–452.

Mori, T., Tanaka, K., Buffo, A., Wurst, W., Kühn, R., and Götz, M. (2006). Inducible gene deletion in astroglia and radial glia–a valuable tool for functional and lineage analysis. Glia *54*, 21–34.

Moss, J., Gebara, E., Bushong, E.A., Sánchez-Pascual, I., O'Laoi, R., El M'Ghari, I., Kocher-Braissant, J., Ellisman, M.H., and Toni, N. (2016). Fine processes of Nestin-GFP-positive radial glia-like stem cells in the adult dentate gyrus ensheathe local synapses and vasculature. Proc. Natl. Acad. Sci. USA *113*, E2536–E2545.

Nakamura, T., Colbert, M.C., and Robbins, J. (2006). Neural crest cells retain multipotential characteristics in the developing valves and label the cardiac conduction system. Circ. Res. *98*, 1547–1554.

Nolte, C., Matyash, M., Pivneva, T., Schipke, C.G., Ohlemeyer, C., Hanisch, U.-K., Kirchhoff, F., and Kettenmann, H. (2001). GFAP promoter-controlled EGFP-expressing transgenic mice: a tool to visualize astrocytes and astrogliosis in living brain tissue. Glia *33*, 72–86.

Oruganty-Das, A., Ng, T., Udagawa, T., Goh, E.L., and Richter, J.D. (2012). Translational control of mitochondrial energy production mediates neuron morphogenesis. Cell Metab. *16*, 789–800.

Perry, S.W., Norman, J.P., Barbieri, J., Brown, E.B., and Gelbard, H.A. (2011). Mitochondrial membrane potential probes and the proton gradient: a practical usage guide. Biotechniques *50*, 98–115.

Pico, A.R., Kelder, T., van Iersel, M.P., Hanspers, K., Conklin, B.R., and Evelo, C. (2008). WikiPathways: pathway editing for the people. PLoS Biol. *6*, e184.

Rafalski, V.A., and Brunet, A. (2011). Energy metabolism in adult neural stem cell fate. Prog. Neurobiol. *93*, 182–203.

Rolando, C., and Taylor, V. (2014). Neural stem cell of the hippocampus: development, physiology regulation, and dysfunction in disease. Curr. Top. Dev. Biol. *107*, 183–206.

Schindelin, J., Arganda-Carreras, I., Frise, E., Kaynig, V., Longair, M., Pietzsch, T., Preibisch, S., Rueden, C., Saalfeld, S., Schmid, B., et al. (2012). Fiji: an open-source platform for biological-image analysis. Nat. Methods *9*, 676–682.

Seib, D.R., Corsini, N.S., Ellwanger, K., Plaas, C., Mateos, A., Pitzer, C., Niehrs, C., Celikel, T., and Martin-Villalba, A. (2013). Loss of Dickkopf-1 restores neurogenesis in old age and counteracts cognitive decline. Cell Stem Cell *12*, 204–214.

Shin, J., Berg, D.A., Zhu, Y., Shin, J.Y., Song, J., Bonaguidi, M.A., Enikolopov, G., Nauen, D.W., Christian, K.M., Ming, G.L., and Song, H. (2015). Single-cell RNA-seq with waterfall reveals molecular cascades underlying adult neurogenesis. Cell Stem Cell *17*, 360–372.

Shook, B.A., Manz, D.H., Peters, J.J., Kang, S., and Conover, J.C. (2012). Spatiotemporal changes to the subventricular zone stem cell pool through aging. J. Neurosci. *32*, 6947–6956.

Silva, J.P., Köhler, M., Graff, C., Oldfors, A., Magnuson, M.A., Berggren, P.O., and Larsson, N.G. (2000). Impaired insulin secretion and beta-cell loss in tissue-specific knockout mice with mitochondrial diabetes. Nat. Genet. *26*, 336–340.

Smith, L.K., He, Y., Park, J.S., Bieri, G., Snethlage, C.E., Lin, K., Gontier, G., Wabl, R., Plambeck, K.E., Udeochu, J., et al. (2015). β2-microglobulin is a systemic pro-aging factor that impairs cognitive function and neurogenesis. Nat. Med. *21*, 932–937.

Sörensen, L., Ekstrand, M., Silva, J.P., Lindqvist, E., Xu, B., Rustin, P., Olson, L., and Larsson, N.G. (2001). Late-onset corticohippocampal neurodepletion attributable to catastrophic failure of oxidative phosphorylation in MILON mice. J. Neurosci. *21*, 8082–8090.

Spalding, K.L., Bergmann, O., Alkass, K., Bernard, S., Salehpour, M., Huttner, H.B., Boström, E., Westerlund, I., Vial, C., Buchholz, B.A., et al. (2013). Dynamics of hippocampal neurogenesis in adult humans. Cell *153*, 1219–1227.

Steib, K., Schäffner, I., Jagasia, R., Ebert, B., and Lie, D.C. (2014). Mitochondria modify exercise-induced development of stem cell-derived neurons in the adult brain. J. Neurosci. *34*, 6624–6633.

Steiner, B., Klempin, F., Wang, L., Kott, M., Kettenmann, H., and Kempermann, G. (2006). Type-2 cells as link between glial and neuronal lineage in adult hippocampal neurogenesis. Glia *54*, 805–814.

Stockburger, C., Kurz, C., Koch, K.A., Eckert, S.H., Leuner, K., and Müller, W.E. (2013). Improvement of mitochondrial function and dynamics by the metabolic enhancer piracetam. Biochem. Soc. Trans. *41*, 1331–1334.

Stoll, E.A., Cheung, W., Mikheev, A.M., Sweet, I.R., Bielas, J.H., Zhang, J., Rostomily, R.C., and Horner, P.J. (2011). Aging neural progenitor cells have decreased mitochondrial content and lower oxidative metabolism. J. Biol. Chem. *286*, 38592–38601.

Stoll, E.A., Makin, R., Sweet, I.R., Trevelyan, A.J., Miwa, S., Horner, P.J., and Turnbull, D.M. (2015). Neural stem cells in the adult subventricular zone oxidize fatty acids to produce energy and support neurogenic activity. Stem Cells *33*, 2306–2319.

Sullivan, L.B., Gui, D.Y., Hosios, A.M., Bush, L.N., Freinkman, E., and Vander Heiden, M.G. (2015). Supporting aspartate biosynthesis is an essential function of respiration in proliferating cells. Cell *162*, 552–563.

Tashiro, A., Zhao, C., and Gage, F.H. (2006). Retrovirus-mediated single-cell gene knockout technique in adult newborn neurons in vivo. Nat. Protoc. *1*, 3049–3055.

Waegemans, T., Wilsher, C.R., Danniau, A., Ferris, S.H., Kurz, A., and Winblad, B. (2002). Clinical efficacy of piracetam in cognitive impairment: a meta-analysis. Dement. Geriatr. Cogn. Disord. *13*, 217–224.

Wang, J., Wilhelmsson, H., Graff, C., Li, H., Oldfors, A., Rustin, P., Brüning, J.C., Kahn, C.R., Clayton, D.A., Barsh, G.S., et al. (1999). Dilated cardiomyopathy and atrioventricular conduction blocks induced by heart-specific inactivation of mitochondrial DNA gene expression. Nat. Genet. *21*, 133–137.

Yamaguchi, M., Saito, H., Suzuki, M., and Mori, K. (2000). Visualization of neurogenesis in the central nervous system using nestin promoter-GFP transgenic mice. Neuroreport *11*, 1991–1996.

Yeo, H., Lyssiotis, C.A., Zhang, Y., Ying, H., Asara, J.M., Cantley, L.C., and Paik, J.H. (2013). FoxO3 coordinates metabolic pathways to maintain redox balance in neural stem cells. EMBO J. *32*, 2589–2602.

Zhang, X., Liu, W., Niu, X., and An, L. (2010). Systemic administration of catalpol prevents D-galactose induced mitochondrial dysfunction in mice. Neurosci. Lett. *473*, 224–228.

Zhao, C., Teng, E.M., Summers, R.G., Jr., Ming, G.L., and Gage, F.H. (2006). Distinct morphological stages of dentate granule neuron maturation in the adult mouse hippocampus. J. Neurosci. *26*, 3–11.

Zheng, X., Boyer, L., Jin, M., Mertens, J., Kim, Y., Ma, L., Ma, L., Hamm, M., Gage, F.H., and Hunter, T. (2016). Metabolic reprogramming during neuronal differentiation from aerobic glycolysis to neuronal oxidative phosphorylation. eLife *5*, e13374.

STAR★METHODS

KEY RESOURCES TABLE

REAGENT or RESOURCE	SOURCE	IDENTIFIER
Antibodies		
rat anti-BrdU	Bio-Rad (formerly Serotec)	AbD Serotec Cat# MCA2060 RRID: AB_323427
mouse anti-BrdU	Millipore	Millipore Cat# MAB3424 RRID: AB_94851
mouse anti-Cox1 (MTCO1)	Abcam	Abcam Cat# ab14705 RRID: AB_2084810
guinea pig anti-DCX	Millipore	Millipore Cat# AB2253 RRID: AB_1586992
chicken anti-GFP	Aves	Aves Labs Cat# GFP-1020 RRID: AB_10000240
rabbit anti-GFP	Invitrogen	Thermo Fisher Scientific Cat# A-11122 RRID: AB_221569
goat anti-HSP60	Santa Cruz	Santa Cruz Biotechnology Cat# sc-1722 RRID: AB_2233354
rabbit anti-Ki67	Millipore	Millipore Cat# AB9260, RRID: AB_2142366
rabbit anti-MCM2	Cell Signaling Technologies	Cell Signaling Technology Cat# 3619S, RRID: AB_2142137
mouse anti-oxPhos	Abcam	Abcam Cat# ab110413, RRID: AB_2629281
mouse anti-Nestin	Millipore	Millipore Cat# MAB353, RRID: AB_94911
rabbit anti-Prox1	Millipore	Millipore Cat# AB5475, RRID: AB_177485
rabbit anti-Stathmin	Abcam	Abcam Cat# ab47468, RRID: AB_882723
rabbit anti-Tbr2	Abcam	Abcam Cat# ab23345, RRID: AB_778267
biotinylated goat anti-GFP	Vector Laboratories	Vector Laboratories Cat# BA-0702, RRID: AB_2336121
DyLight 405-conjugated donkey anti-rabbit	Jackson Laboratories	Jackson ImmunoResearch Labs Cat# 711-475-152, RRID: AB_2340616
AMCA-conjugated donkey anti-guinea pig	Jackson Laboratories	Jackson ImmunoResearch Labs Cat# 706-155-148, RRID: AB_2340458
Cy3-conjugated donkey anti-rat	Jackson Laboratories	Jackson ImmunoResearch Labs Cat# 712-165-153, RRID: AB_2340667
Cy3-conjugated donkey anti-rabbit	Jackson Laboratories	Jackson ImmunoResearch Labs Cat# 711-165-152, RRID: AB_2307443
Cy3-conjugated donkey anti-goat	Jackson Laboratories	Jackson ImmunoResearch Labs Cat# 705-165-147, RRID: AB_2307351
FITC-conjugated donkey anti-chicken	Jackson Laboratories	Jackson ImmunoResearch Labs Cat# 703-095-155, RRID: AB_2340356
Alexa 488-conjugated donkey anti-mouse	Invitrogen	Thermo Fisher Scientific Cat# A-21202, RRID: AB_2535788
Cy5-conjugated donkey anti-mouse	Jackson Laboratories	Jackson ImmunoResearch Labs Cat# 715-175-151, RRID: AB_2340820
Cy5-conjugated donkey anti-goat	Jackson Laboratories	Jackson ImmunoResearch Labs Cat# 705-175-147, RRID: AB_2340415
Cy5-conjugated donkey anti-rabbit	Jackson Laboratories	Jackson ImmunoResearch Labs Cat# 711-175-152, RRID: AB_2340607
biotinylated donkey anti-chicken	Jackson Laboratories	Jackson ImmunoResearch Labs Cat# 703-065-155, RRID: AB_2313596
biotinylated donkey anti-mouse	Jackson Laboratories	Jackson ImmunoResearch Labs Cat# 715-065-151, RRID: AB_2340785
biotinylated goat anti-rabbit	Jackson Laboratories	Jackson ImmunoResearch Labs Cat# 111-066-047, RRID: AB_2337969
Alexa 488-Streptavidin	Invitrogen	Thermo Fisher Scientific Cat# S11223, RRID: AB_2336881

(*Continued on next page*)

Continued

REAGENT or RESOURCE	SOURCE	IDENTIFIER
Cy3-Streptavidin	Jackson Laboratories	Jackson ImmunoResearch Labs Cat# 016-160-084\\t, RRID: AB_2307342
Cy5-Streptavidin	Jackson Laboratories	Jackson ImmunoResearch Labs Cat# 016-170-084, RRID: AB_2337245
gold-conjugated goat anti-rabbit	Nanoprobes	Nanoprobes Cat# 2004, RRID: AB_2631182
Chemicals, Peptides, and Recombinant Proteins		
BrdU	Sigma-Aldrich	Cat#: B5002
Rotenon	Sigma-Aldrich	Cat#: R8875
Oligomycin	Sigma-Aldrich	Cat#: 75351
Piracetam	Sigma-Aldrich	Cat#: P5295
BMP4	R&D Systems	Cat#: 5020-BP
Accutase	Millipore	Cat#: SCR005
Rhodamin-123	Sigma-Aldrich	Cat#: R8004
Trypan Blue	Sigma-Aldrich	Cat#: T8154
Critical Commercial Assays		
Avidin biotinperoxidase complex (ABC Elite)	Vector Laboratories	PK-6100
DAB	Vector Laboratories	SK-4100
HQ Silver Kit	Nanoprobes	#2012
MACS Neural Tissue Dissociation Kit	Miltenyi Biotec	Cat#: 130-092-628
Bioluminescence Assay	ViaLight Kit Lonza	Cat#: LT07-221
ApoTag Red in Situ Apoptosis Detection Kit	Millipore	Cat#: S7165
Deposited Data		
Single cell sequencing data	Shin et al., 2015	GEO: GSE71485
Experimental Models: Organisms/Strains		
$Tfam^{loxP/loxP}$ mouse; B6.Cg-*Tfamtm1.1Ncdl*/J	Larsson et al., 1998	N/A
GLAST::$CreER^{T2}$ mouse; Tg(Slc1a3-cre/ERT)1Nat/J	Mori et al., 2006	N/A
CAG-CAT-eGFP mouse; FVB.B6-Tg(CAG-cat,-EGFP)1Rbns/KrnzJ	Nakamura et al., 2006	N/A
hGFAPeGFP mouse; FVB/N-Tg(GFAPGFP)14Mes/J	Nolte et al., 2001	N/A
Nestin-GFP mouse; B6.Cg-Tg(Nes-EGFP)1Yamm	Yamaguchi et al., 2000	N/A
C57BL/6 mouse	Charles River	Strain code: 027
NMRI	Charles River	N/A
Recombinant DNA		
MMLV pCAG-GFP	Zhao et al., 2006	Addgene 16664
MMLV pCAG-GFP-IRES-Cre	Zhao et al., 2006	Addgene 48201
Sequence-Based Reagents		
Tfam-A CTGCCTTCCTCTAGCCCGGG	Life Technologies	N/A
Tfam-B GTAACAGCAGACAACTTGTG	Life Technologies	N/A
Tfam-C CTCTGAAGCACATGGTCAAT	Life Technologies	N/A
Software and Algorithms		
Fiji ImageJ software	Schindelin et al., 2012	https://fiji.sc/
Custom R Code for Hidden Markov Model	Shin et al., 2015	http://doi.org/10.1016/j.stem.2015.07.013 Data S1
Reconstruct Software	Fiala, 2005	http://www.bu.edu/neural/Reconstruct.html
Adobe Creative Suite	Adobe	http://www.adobe.com/creativecloud.html
Imaris software	Bitplane	http://www.bitplane.com/
XLStat	Addinsoft	https://www.xlstat.com/en/download

CONTACT FOR REAGENT AND RESOURCE SHARING

Further information and requests for reagents may be directed to and will be fulfilled by the Lead Contact, Dr. Chichung Lie (chi.lie@fau.de).

EXPERIMENTAL MODEL AND SUBJECT DETAILS

All experiments were carried out in accordance with the European Communities Council Directive (86/609/EEC). Animal experiments were approved by the Governments of Upper Bavaria, Middle-Franconia, and Hesse.

For all experiments, mice were group housed in standard cages under a 12 hr light/dark cycle with ad libitum access to water and food. *Tfam*$^{loxP/loxP}$ mice (Larsson et al., 1998), *GLAST::CreER*^{T2} (Mori et al., 2006), *CAG-CAT-EGFP* reporter mice (Nakamura et al., 2006), and *hGFAPeGFP* (Nolte et al., 2001) served for the characterization of in vivo phenotypes and in vitro studies. For EM-studies, *Nestin-GFP* mice (Yamaguchi et al., 2000) and C57BL/6 (Charles River, Sulzfeld, Germany) were used. For piracetam experiments, we injected NMRI mice (Charles River, Sulzfeld, Germany). All animals have been described previously.

METHOD DETAILS

Tissue processing

Animals were sacrificed using CO_2. Mice were transcardially perfused with 50 mL phosphate-buffered saline (PBS, pH 7.4) followed by 100 mL 4% paraformaldehyde (PFA) at a rate of 10 mL/min. Brains were postfixed in 4% PFA for 12 hr at 4°C and were subsequently transferred to a 30% sucrose solution. Coronal brain sections were produced using a sliding microtome (Leica Microsystems, Wetzlar, Germany) for phenotyping and morphological analysis.

Tfam genotyping

The following primers were used for genotyping *Tfam*^{cko} mice and cells: Tfam-A CTGCCTTCCTCTAGCCCGGG, Tfam-B GTAACAG CAGACAACTTGTG, Tfam-C CTCTGAAGCACATGGTCAAT.

EM processing

To analyze NSCs of the dorsal dentate gyrus, tissue from transgenic *Nestin-GFP* mice was processed as previously described (Moss et al., 2016). Briefly, male mice (P83-88) were anaesthetised, transcardially perfused with phosphate-buffered saline (PBS) then fixative, and placed at 4°C for 24 hr. Brains were post-fixed for 24 hr at 4°C, washed in PBS, and cut in 50 μm coronal sections. Sections were washed in PBS, incubated in cryoprotectant (2 h; room temperature; r.t.), freeze-thawed and Nestin-GFP revealed with immuno-peroxidase or -gold.

For the immunoperoxidase (IP) processing, an overnight incubation (r.t.) with a rabbit anti-GFP primary antibody (1:1000; Invitrogen) was followed by 2 hr incubation (r.t) in a secondary antibody (biotinylated goat anti-rabbit; 1:200; Jackson Laboratories). Incubation in avidin biotin peroxidase complex (ABC Elite; Vector Laboratories; 90 min; r.t.) and washes in 0.05 M Tris-buffered saline (Sigma) preceded the peroxidase reaction with 3, 3-diaminobenzidine as the chromogen (DAB; Vector Laboratories Kit; 4-6 min reaction).

For the immunogold (IG) processing, the sections were incubated overnight (r.t.) in the primary antibody (rabbit anti-GFP; 1:1000; Invitrogen) and for 2 hr (r.t.) in the gold-conjugated secondary antibody (goat anti-rabbit; 1:100; Nanoprobes; 1.4 nm colloidal gold). Sections were then washed in PBS and 0.1 M sodium acetate 3-hydrate buffer (Sigma), before the gold particles were silver intensified (HQ Silver Kit; Nanoprobes; 3-5 min).

To analyze IPCs, C57BL/6 female mice (P56-70) were stereotaxically injected with a recombinant MML-retrovirus encoding for GFP (pCAG-GFP), as previously described (Zhao et al., 2006). Two days after injection, mice were transcardially perfuse-fixed and their brains IP processed (as for NSC tissue) to reveal GFP labeling of IPCs for EM. In place of primary and secondary antibodies, a biotinylated primary antibody was used to improve labeling efficacy (biotinylated rabbit anti-GFP, Vector Laboratories, 1:1000).

Both IP- and IG-labeled sections, containing NSCs or IPCs, were then prepared for EM. Sections were post-fixed with 1% osmium tetroxide (Electron Microscopy Sciences; 30 min for IP-labeling, 7 min for IG-labeling), and then dehydrated in an ascending series of ethanol dilutions [50%, 70% (with 1% uranyl acetate; w/v; Electron Microscopy Sciences), 95% and 100%] and acetone. Sections were then lifted into resin (Durcupan ACM, Fluka), left overnight (r.t.), then placed on microscope slides, coverslipped, and the resin cured at 65°C for 3 d.

Regions of interest were identified at the light microscope level, then tissue was cut from the slide and serial ultrathin sections (70 nm) were cut and collected onto Formvar-coated, single-slot copper grids (Electron Microscopy Sciences). The tissue was then contrasted with lead citrate and examined using a Philips CM10 transmission electron microscope (Electron Microscope Facility at the University of Lausanne). Images were captured using a digital camera (Morada SIS, Olympus), processed using Adobe Creative Suite and analyzed/3D-reconstructed using Fiji ImageJ software.

To analyze newborn neurons, MML-retroviral birthdating using the pCAG-GFP vector was used (Zhao et al., 2006). Briefly, adult C57BL/6 female mice (30 d after viral injection at P4) were perfused with saline then PBS-containing fixative, and their brains cut in 100 μm coronal sections. Under a fluorescence microscope, 1-2 cells per mouse were injected with 5% aqueous Lucifer yellow (Sigma). Sections were incubated with 2.8 mM DAB and 6 mM potassium cyanide, and irradiated under epifluorescence using a 75-W Hg to induce photo-conversion of DAB into an electron-dense residue. Sections were then post-fixed overnight in a solution of 3% glutaraldehyde and processed for electron microscopy as for NSC/IPC tissue. Serial sections of labeled dendritic segments were cut longitudinally at a thickness of 40 nm and imaged with a Megaview III camera mounted on a JEOL 100CXII electron microscope. Images were processed using Adobe Photoshop, aligned using Align software (J. Fiala, Boston University) and analyzed/3D-reconstructed using Fiji ImageJ.

In vitro assays

Neural stem/progenitor cell (NSPC) isolation

NSPCs were isolated from the DG of 8 weeks-old *Tfam*$^{fl/fl}$ mice and from the forebrain of 4 months and 1 year-old *hGFAPeGFP* mice with the MACS neural tissue dissociation kit according to manufacturer's protocol (MACS Miltenyi Biotec). Cells were kept in proliferative growth medium consisting of DMEM F12 Glutamax (GIBCO) medium with 1xNeurobrew-21 (MACS Miltenyi Biotec), 1xPSF (GIBCO) 8 mM HEPES and 10 ng/ml EGF and 10 ng/ml FGF (Peprotech) and were grown as neurospheres.

KO induction of Tfam$^{loxP/loxP}$ cells

Tfam$^{loxP/loxP}$ NSPCs were grown as neurospheres, dissociated with Accutase (Millipore) into single cells. Two million cells were seeded in 10 mL growth medium on 10 cm tissue culture plates coated with PDL/Laminin. After 24 hr cells were transduced with a GFP encoding control MML-retrovirus or a MML-retrovirus bi-cistronically encoding for Cre recombinase and GFP. Transduction was repeated 3 days later. Cells were harvested the next day and subsequently used in experiments. Recombination was confirmed via genotyping PCR.

BMP4-treatment

NSPCs were grown as neurospheres, dissociated with Accutase (Millipore) into single cells and seeded according to experiments. After 3 hr cells were treated with 20 ng/ml BMP4 (R&D Systems). Experiments were started 24 hr after exposure to BMP4.

Treatment with Rotenon, Oligomycin and piracetam

NSPCs were grown as neurospheres, dissociated with Accutase (Millipore) into single cells and seeded on PDL/Laminin coated tissue culture plates. Seeding densities are listed in the respective experiments. After 24 hr cells were incubated with either 1 μM Rotenon, 3.8 μM Oligomycin, and/or 1 mM piracetam for 24 hr prior to analysis.

Mitochondrial Membrane Potential Measurement

NSPCs were dissociated with Accutase into single cells and were seeded in 0.5 mL of growth medium at a density of 200,000 cells/well onto a 24-well tissue culture plate coated with PDL/Laminin. After 24 hr cells were treated as indicated. 24 hr later 0.4 M Rhodamin-123 was added for 15 min at 37°C. 500 μl HBSS was added and the plate was centrifuged at 1500 rpm for 5 min. Supernatant was removed, 500 μl HBSS was added and the fluorescence signal was measured using aVICTORX2Multilabel Plate Reader (Perkin Elmer) at 490/535 nm. The transmembrane distribution of the Rhodamin-123 dye is proportional to strength of the membrane potential.

ATP Measurement

ATP levels were determined using a bioluminescence Assay (ViaLight Plus® Kit). The assay is based on a luciferase reaction, which catalyzes the formation of light from ATP and luciferin. NSPCs were dissociated with Accutase into single cells. Cells were seeded in 100 μl of growth medium at a density of 40,000 cells/well onto a white-walled 96 well plate coated with PDL/Laminin. After 24 hr cells were treated as indicated. 24 hr later cells were processed according to the manufacturer's instructions. The emitted light, which is linearly proportional to the ATP concentration, was measured with a VICTOR X2 Multilabel Plate Reader (Perkin Elmer). Amount of ATP per 40,000 cells was determined by interpolation according to an ATP standard.

Proliferation Assay

NSPCs were dissociated with Accutase into single cells. Cells were seeded in 1 mL growth medium at a density of 100,000 cells / well onto a 24-well tissue culture plate coated with PDL/Laminin. 24 hr later, cells were treated with 5 mM BrdU for 2 hr prior to fixation with 4% PFA. Immunocytochemistry was performed as previously described (Lie et al., 2002). All quantifications were performed in a blinded fashion.

Viability Assay

NSPCs were dissociated with Accutase into single cells, seeded in 1 mL growth medium at a density of 50,000 cells/well onto a 24-well tissue culture plate, and treated as indicated. 24 hr later, 15 μl of the cell suspension were mixed with 15 μl of Trypan blue. The number of dead and living cells was determined under a fluorescent microscope with a Neubauer counting chamber and the cell death rate was calculated as the ratio of dead cells per total number of cells (dead + living cells). All quantifications were performed in a blinded fashion.

Histology and counting procedures

The following primary antibodies were used: mouse anti-Cox1 (MTCO1) (1:500; Abcam), goat anti-HSP60 (1:500; Santa Cruz), mouse anti-mitochondrial complexes I-V (oxPhos) mix (1:500; Abcam) chicken anti-GFP (1:2000; Aves), rat anti-BrdU (1:200; Serotec), rabbit

anti-GFP (1:500; Invitrogen), mouse anti-BrdU (1:200; Millipore), rabbit anti-MCM2 (1:200, Cell Signaling Technologies), mouse anti-Nestin (1:200; Millipore), rabbit anti-Tbr2 (1:500; Abcam), guinea pig anti-DCX (1:500; Millipore), anti-rabbit Stathmin (1:20000; Abcam), rabbit anti-Ki67 (1:200; Millipore), rabbit anti-Prox1 (Millipore, 1:2000).

Primary antibodies were visualized with Fluorophore-conjugated secondary antibodies (all 1:400; see Key Resource Table). Biotinylated secondary antibodies (1:400; see Key Resource Table) were used in combination with Fluorophore-conjugated to Streptavidin (1:400; see Key Resource Table) to enhance the signal of GFP, HSP60, Cox1 and mitochondrial complex I-V mix. As a negative control, staining was done using secondary antibody only.

Immunofluorescent stainings were performed on free-floating 40 and 50 μm sections. Slices were washed 3 times with PBS and incubated with primary antibodies in PBS containing 0.5% Triton X-100 and 10% normal donkey serum (NDS) for 72 hr at 4°C. After incubation with the primary antibody, tissue was thoroughly washed with PBS at room temperature and subsequently incubated with the secondary antibody in PBS containing 0.5% Triton X-100 and 10% NDS overnight at 4°C or 2 hr at room temperature. After washing thoroughly in PBS, nuclei were stained with DAPI and sections were mounted on coverslips with Aqua poly mount (Polysciences).

For BrdU staining, tissue was pre-treated in 2M HCL for 30 min, washed shortly in PBS, incubated in Borate buffer (0.1 M, pH 8.5) two times for 15 min, followed by washing with PBS before adding the BrdU antibody.

For immunostainings against mitochondrial markers Cox1, HSP60, and mitochondrial complexes I-V mix, sections were subjected to antigen retrieval. Slices were incubated in Tris-EDTA/Tween20 for 5 min at 99°C and washed 3 times with MilliQ water followed by one washing step with PBS prior incubation with primary antibody.

Confocal single plane images and Z stacks were taken at the Zeiss LSM 780 with four lasers (405, 488, 559, and 633nm) and 63x objective lens and Leica SP5 equipped with four laser lines (405, 488, 559 and 633nm) and 63x and 40x objective lens. Images were processed using using Fiji ImageJ. 3D reconstructions were obtained by using Imaris software (Bitplane AG, Zürich, Switzerland).

Cell death analysis

ApopTag Red in Situ Apoptose Detection Kit (Millipore) was used for cell death anaylsis. Free floating sections from ctrl and *Tfam*^{cko} mice were processed according to the manufacturer's protocol of fluorescent staining of tissue cryosections.

BrdU administration

For proliferation and survival studies, animals were intraperitoneally injected with a single dose of Bromodeoxyuridine (BrdU, 50 mg/kg body weight, Sigma-Aldrich) per day. BrdU was dissolved in 0.9% NaCl and sterile filtered.

To measure proliferation in 4 month-old *Tfam*^{cko} and control mice, mice received a single dose of BrdU 3h prior to perfusion. To compare proliferation between young (4 month-old) and middle-aged (one year-old) mice, mice received daily injections of BrdU for seven consecutive days and were sacrificed 2h after the last injection.

Piracetam administration

Eighteen month-old wild-type NMRI mice received freshly prepared piracetam (2-oxo-1-pyrrolidine-acetamide; 500 mg/kg body weight) administered by gavaging once per day for 14 consecutive days. Control mice (18 month-old wild-type NMRI) received a comparable amount of water by gavage. Animals were perfused one day after the last administration.

Retrovirus preparation and stereotactic injections

MML-retroviruses were generated as previously described (Tashiro et al., 2006). Viral titers were approximately 2x10^8 colony-forming units (cfu) ml^{-1}. 8 week-old *Tfam*$^{loxP/loxP}$ mice were stereotactically injected with the pCAG-GFP-IRES-Cre retrovirus to induce recombination of the conditional *Tfam* locus in highly proliferative precursors of the DG. 8 week-old *Tfam*$^{loxP/loxP}$ mice injected with the pCAG-GFP retrovirus (Zhao et al., 2006) served as controls. The pCAG-GFP retrovirus was also used to birthdate and label newborn neurons for morphology analysis in 2 month- and 8 month-old C57/Bl6 mice.

For stereotactic injections, mice were deeply anesthetized by injecting Fentanyl (0.05 mg/kg; Janssen-Cilag AG, New Brunswick, USA), Midazolam (5 mg/kg; Dormicum, Hoffmann-La Roche, Basel, Switzerland) and Medetomidine (0.5 mg/kg; Domitor, Pfizer Inc., New York, USA) dissolved in 0.9% NaCl. Mice were stereotactically injected with 0.9 μl the retroviruses with a titer of 1 × 10^8 cfu × ml^{-1} into the left and right dentate gyrus (coordinates from bregma were −1.9 anterior/posterior, ± 1.6 medial/lateral, −1.9 dorsal/ventral from dura). Anesthesia was antagonized by injecting Buprenorphine (0.1 mg/kg, Temgesic, Essex Pharma GmbH, Munich, Germany), Atipamezol (2.5 mg/kg; Antisedan, Pfizer Inc., New York, USA) and Flumazenil (0.5 mg/kg; Anexate, Hexal AG, Holzkirchen, Germany) dissolved in 0.9% NaCl.

QUANTIFICATION AND STATISTICAL ANALYSIS

EM mitochondrial volume analyses

Using the serial EM images collected, mitochondrial volumes were analyzed for NSC cell bodies (29 mitochondria, from 2 cells of 2 animals), NSC primary processes (36 mitochondria, 3 cells, 3 animals), NSC fine processes (36 mitochondria, 6 cells, 5 animals), IPC cell bodies (20 mitochondria, 2 cells, 1 animal), IPC primary processes (20 mitochondria, 1 cell, 1 animal) and nb neuron dendrites (30

mitochondria, 4 cells, 4 animals). Mean volumes were calculated and expressed ± SEM (standard error of the mean), and compared using a One-Way ANOVA and post hoc Tukey's Test ($F_{(5, 164)} = 12.02$, $p < 0.0001$).

Analysis of transcriptomic resource

A detailed description of the resource describing the transcriptomic dynamics of early adult hippocampal neurogenesis is provided in the publication by Shin and colleagues (Shin et al., 2015). For functional gene expression analysis, we first divided the entire transcriptome into three equal number of groups based on their Spearman correlation to pseudotime: positively correlated genes, no correlated genes, and negatively correlated genes. We then evaluated the proportion of positively correlated genes versus negatively correlated genes within each functional entity from an independent functional annotation database called wikipathway (Pico et al., 2008). If a functional entity contained disproportionally larger number of upregulated genes than downregulated genes, we could assume that the functional entity is generally activated during early neurogenesis. In contrast, if a GO term contained disproportionally larger number of downregulated genes than upregulated genes, we could assume the pathway is generally inactivated during early neurogenesis.

We used custom R code to apply Hidden Markov model (HMM) to predict gene expression states throughout pseudotime. Briefly, we divided pseudotime into 40 bins, each of which contains average 2.5 single cells. We averaged the expression level within each bin and assigned the expression values to observed variables for HMM. We used Baum-Welch algorithm to extract most probable emission probabilities and transition probabilities without inputting any arbitrary parameters. Using the output from Baum-Welch algorithm along with the observed variables, we applied Viterbi algorithm to predict the hidden gene expression states.

Expression analysis of stage-specific markers

Stage-specific marker expression (Nestin, MCM2, Tbr2, DCX, Prox1, GFAP etc. > 50 cells/per animal and marker) was analyzed by confocal microscopy in at least four sections containing the dentate gyrus from n = 3-7 different animals (as indicated in the figure legends, and in Table S1).

All quantifications were done in a blinded fashion.

In the in vivo piracetam experiment, one piracetam-treated animal was excluded from the analysis of DCX marker expression (Figure 5K) because of a lack of reproducible DCX immunostaining.

Dendritic morphology analyses

To analyze dendrite morphology, confocal images of transduced cells expressing GFP or of cells stained against DCX (for Piracetam experiments) were obtained with a 63 × glycerol objective using a Leica TCS Sp5 confocal microscope (Leica Microsystems, Wetzlar, Germany) (step size 0.3 μm, resolution 1024 × 1024). For the analysis of dendrite morphology in *Tfam*^{cko} mice, 100 μm thick sections were used. For the comparative retrovirus-based analysis of dendrite morphology in young and middle-aged mice, 60 μm thick sections were used. For the DCX-based analysis of dendrite morphology in the piracetam experiment, 40 μm thick sections from a comparable hippocampal position were used. 14-26 cells per group from at least 3 different animals were analyzed. 3D reconstructions were obtained by using the Filament Tracer tool in Imaris (Bitplane AG, Zürich, Switzerland), and values for total dendritic length, number of branch points and number of Scholl intersections were determined.

All quantifications were done in a blinded fashion.

Statistical analysis

Significance levels were assessed using unpaired Student's t test with unequal variances; for quantification of mitochondrial volume we applied One-Way ANOVA with post hoc Tukey's multiple comparisons test to determine significance. Differences were considered statistically significant at $^{*}p < 0.05$, $^{**}p < 0.01$ and $^{***}p < 0.001$. All data are presented as mean ± SEM (standard error of the mean).

DATA AND SOFTWARE AVAILABLILTY

Custom R code to apply Hidden Markov model (HMM) to predict gene expression states throughout pseudotime can be found online at http://dx.doi.org/10.1016/j.stem.2015.07.013 in Data S1 (Shin et al., 2015).